

Lumped and Distributed Device Embedding Techniques
in Time Domain TLM Field Models

by
Jong Woon Park

B. Eng., University of KyungHee, 1999

A Thesis Submitted in Partial Fulfillment of the
Requirements for the Degree of

MASTER OF APPLIED SCIENCE

in the Department of
Electrical and Computer Engineering

We accept this thesis as conforming
to the required standard

Dr. W. J. R. Hoefer, Supervisor (Dept. of Elec. and Comp. Eng.)

Dr. M. A. Stuchly, Departmental Member (Dept. of Elec. and Comp. Eng.)

Dr. J. Bornemann, Departmental Member (Dept. of Elec. and Comp. Eng.)

Dr. J. W. Provan, Outside Member (Dept. of Mech. Eng.)

Dr. D. Olesky, External Examiner (Dept. of Comp. Sc.)

© Jong Woon Park, 2001
UNIVERSITY OF VICTORIA

*All rights reserved. This thesis may not be reproduced in whole or in part,
by any means, without the permission of the author.*

QC665
E4P37

201
201

201

201
201

Supervisor: Dr. W. J. R. Hoefler

ABSTRACT

The TLM method has the advantage that electromagnetic field equations are modeled by means of transmission line networks. Therefore, embedding of lumped and distributed devices in the TLM mesh is straightforward since the equivalent models of those can be connected to a TLM node using transmission lines. In this thesis, several techniques for spreading the device over a finite volume corresponding to its physical size are presented. In order to connect the device to the TLM network, the equations governing the devices are solved using a central difference scheme. However, this approach is time consuming and requires extra programming effort, especially for a nonlinear active device. The connection between SPICE and TLM enables us to overcome the encountered problems. The main benefit of such a hybrid system is to take advantage of the efficient combination of their respective strengths to solve complex electromagnetic problems and enhance computational efficiency.

Examiners:

Dr. W. J. R. Hoefler, Supervisor (Dept. of Elec. And Comp. Eng.)

Dr. M. A. Stuchly, Departmental Member (Dept. of Elec. And Comp. Eng.)

Dr. J. Bornemann, Departmental Member (Dept. of Elec. And Comp. Eng.)

Dr. J. W. Provan, Outside Member (Dept. of Mech. Eng.)

Dr. D. Olesky, External Examiner (Dept. of Comp. Sc.)

Table of Contents

Abstract	ii
Table of Contents	iii
List of Figures	v
List of Tables	viii
List of Common Symbols	ix
Acknowledgment	x
1. Research Objectives	
1.1 Introduction	1
1.2 Research Objectives	4
1.3 Original Contributions	5
1.4 Preview of Contents	5
2. The Transmission Line Matrix Method	
2.1 Introduction	7
2.2 Shunt-Connected 2D-TLM Network	9
2.3 The 3D-TLM Network	14
2.4 Characteristics of the TLM Method and Sources of Errors	20
2.5 Conclusion	22
3. Review of Non-Linear Device Characteristics and their Circuit Models	
3.1 Introduction	23
3.2 <i>P-N</i> Junction Diode	24
3.3 Tunnel Diode	25
3.4 Bipolar Junction Transistor	27
3.5 Conclusion	28
4. Lumped and Distributed Device Embedding Techniques	
4.1 Introduction	29
4.2 Node Implementation	33
4.3 Boundary Implementation	41
4.4 Star-Type Implementation	44
4.5 Conclusion	45

5. Comparison of Device Embedding Techniques	
5.1 Introduction	47
5.2 Modeling of Linear First-Order Devices	48
5.3 Modeling of Nonlinear Passive and Active Devices	53
5.4 Conclusion	60
6. The Connection between SPICE and TLM	
6.1 Introduction	61
6.2 Connection between SPICE and TLM	62
6.3 Validation of the SPICE-TLM Algorithm	64
6.4 Conclusion	72
7. Discussion and Future Work	
7.1 Introduction	73
7.2 Future Work	75
7.3 Overall Conclusion	76
Bibliography	78

List of Figures

Figure 2.1	The description of the scattering and connection process of the TLM algorithm (a) Injection of impulse voltage (b) Scattering at the node (c) Connection to the neighboring nodes	9
Figure 2.2	2D-TLM shunt node (a) TLM cell (b) its lumped element equivalent circuit	10
Figure 2.3	SCN mesh	15
Figure 3.1	I-V characteristic of tunnel diode	26
Figure 3.2	Ebers-Moll large-signal model of a Bipolar Junction Transistor	27
Figure 4.1	Typical node and boundary implementations of lumped devices in a TLM mesh. (a) Single Node implementation (b) 1x1 boundary implementation (c) 3x3 node implementation (d) 3x3 boundary implementation (e) 3x3 Star-type implementation. The mesh size is the same ($\Delta l=1\text{mm}$) in all cases. The 50Ω parallel plate waveguide is $31 \Delta l$ wide	30
Figure 4.2	(a) The ideal equivalent circuit of a 50Ω resistance in a transmission line (b) Equivalent circuit of a 50Ω resistive post in a parallel plate waveguide with 50Ω characteristic impedance, including parasitic reactances.	31
Figure 4.3	S-Parameters of a lumped 50 Ohm resistor placed in a matched 50 Ohm parallel plate waveguide computed with TLM using different implementations outlined in Figure 4.1	32
Figure 4.4	Models for connecting lumped elements to a TLM network: (a) link-line connection, (b) node connection with device stub of length $\Delta l/2$ and (c) node connection with device stub of length zero. The TLM link lines are numbered 1 - 5	33
Figure 4.5	A lumped device connected in parallel to a 2D-TLM shunt node	35
Figure 4.6	A device volume occupying $W\Delta x * H\Delta y * l\Delta z$. Each sub-device is connected to the corresponding node	36
Figure 4.7	A single element connected to 3D-TLM mesh by means of the stacked stubs in the direction of the feeding voltage (V_y)	38
Figure 4.8	The stacked stub arrangement (a) and its Thevenin equivalent circuit (b). Z_s is the characteristic impedance of the stubs	38
Figure 4.9	A schematic connection of a two-port device in the z-direction by two sets of stacked stubs	40

Figure 4.10	The layout of sub-devices in boundary implementation using 2D-TLM shunt node	42
Figure 4.11	A schematic connection of a two-port device in the z-direction by two sets of stacked link lines	43
Figure 4.12	A schematic layout of star-type implementation in 2D-TLM shunt node	44
Figure 5.1	The geometry of a parallel-plate waveguide containing device volume (a) and its 1D equivalent circuit (b)	49
Figure 5.2	S-parameters of low-pass filter (a) and high-pass filter (b)	50
Figure 5.3	The S-parameters of the band-stop filter	52
Figure 5.4	(a) The transmission line oscillator (b) stacked biasing circuit of height h	53
Figure 5.5	Equivalent DC circuit of the push-pull transmission-line oscillator. This circuit is only valid at dc.	54
Figure 5.6	I-V characteristic of a tunnel diode and its biasing point	54
Figure 5.7	Transient behavior and frequency response of the push-pull oscillator by 3D-TLM network (dotted line : 1*1, solid line : 3*3)	56
Figure 5.8	Time domain responses of a tunnel diode obtained with the node and boundary device embedding techniques	57
Figure 5.9	Comparison of the transient behavior and frequency response of the push-pull diode simulated by the node (dotted line) and star-type device embedding technique (solid line) in 2D-TLM	57
Figure 5.10	Frequency response of a p-n junction diode obtained by the star-type device embedding technique in 2D-TLM	59
Figure 6.1	The schematic in SPICE for one-port (a) and two-port (b) devices	62
Figure 6.2	The flow chart representing the coupling SPICE with TLM network	63
Figure 6.3	The S-parameters of the high-pass filter obtained by SPICE-TLM, SPICE-FDTD and Theory.	64

- Figure 6.4 The S-parameters and their phases obtained by SPICE-TLM (solid line) and Theory (dotted line) 65
- Figure 6.5 A simple amplifier with a BJT transistor 67
- Figure 6.6 The base-emitter voltage computed with SPICE alone (dash dotted line), SPICE-TLM using node implementation (solid line), and SPICE-TLM using boundary implementation (dotted line). 68
- Figure 6.7 The collector-emitter voltage computed with SPICE alone (dash dotted line), SPICE-TLM using node implementation (solid line), and SPICE-TLM using boundary implementation (dotted line). 68
- Figure 6.8 The base-emitter voltage computed with SPICE alone (dotted line), SPICE-TLM using node implementation (solid line), and SPICE-TLM using boundary implementation (dash dotted line). 70
- Figure 6.9 The collector-emitter voltage computed with SPICE alone (dotted line), SPICE-TLM using node implementation (solid line), and SPICE-TLM using boundary implementation (dash dotted line). 70

List of Table

Table 1 Specifications of the Tunnel diodes used in the oscillator in Figure 5.4

53

List of Common Symbols

$\Delta x, \Delta y, \Delta z, \Delta l, \Delta t$	Space and time step sizes [m], [s]
v_l, v_{TL}	Phase velocity of the transmission line [m/s]
v_n	Phase velocity of the TLM network [m/s]
Z_l	Characteristic impedance of the transmission line [Ω]
Z_n	Characteristic impedance of the TLM network [Ω]
c	Velocity of light [m/s]
k	Time index variable
x, y, z, t	Space and time coordinates [m], [s]
${}_k V^r, {}_k V^i$	Reflected and incident voltages at $t = k \Delta t$
L, C	Inductance and capacitance [H], [F]
ϵ, μ	Permittivity and permeability of a medium [F/m], [H/m]
σ	Conductivity of a medium [S/m]
E_x, E_y, E_z	Electric field components [V/m]
H_x, H_y, H_z	Magnetic field components [A/m]
V, I	Voltage and current [V], [A]
[S]	Scattering matrix
Y_s	Characteristic admittance of the device stub [\square]
f	Frequency [Hz]
SPICE	Simulation Program with Integrated Circuit Emphasis

Acknowledgment

I thank Dr. Hofer and my research group members for their help with my studies and research.

Chapter 1

Research Objectives

1.1 Introduction

Electromagnetic problems may be solved using several techniques. These techniques can be classified as experimental, analytical, or numerical. Experimental techniques are not used very often since they are very expensive, time consuming, and do not allow much flexibility in parameter variations. They serve mainly to validate analytical or numerical solution. Analytical methods are still used in solving field problems. These [1] include Separation of Variables, Series Expansion, Fourier Transformation, Perturbation Method, etc. It is not easy, however, to apply them to the problems involving complex geometry.

Numerical techniques have been thoroughly studied in the past three decades. Due to the necessity of developing and researching microwave and RF devices, electromagnetic interference, IC circuits, antenna design, etc, numerical techniques have

become an important research topic. Numerical methods are used to characterize and model problems that cannot be solved analytically.

Numerical methods [2] include Finite Difference, Finite Element, Transmission Line Matrix (TLM) methods, the Method of Moments, Mode-Matching, and the Spectral Domain Approach. The first three methods are derived from the differential or integral form of Maxwell's equations and require the discretization of the computation region. These methods lead to identical discrete algorithms for field computation under certain condition [3]. The last three methods are mostly based on the integral form of Maxwell's equations and require some analytical preprocessing. The numerical solution of large electromagnetic problems can require huge storage and CPU time. Therefore, numerical methods are chosen on the basis of trade-offs between accuracy, speed, storage requirement, versatility, etc.

For instance, field problems involving layered structures with simple boundaries can be resolved efficiently by spectral domain methods since considerable analytical preprocessing reduces the computational effort and simplifies the data input and output procedures. These methods have some disadvantages. They cannot take time-dependent properties into account and also cannot be applied to structures of complex and irregular cross sections. Time domain numerical techniques, such as TLM and FDTD, are capable of tackling these problems. These methods are useful in dealing with complex, closed boundary, heterogeneous media structures. They also account for transient effects, electromagnetic coupling and interference.

The TLM (Transmission Line Matrix) method [4][5], which models wave propagation by an equivalent spatial network based on Huygen's principle, has become

increasingly popular for the computation of electromagnetic wave propagation and scattering problems. It is based on the equivalence between Maxwell's equations and the equations for voltages and currents on a mesh of transmission lines. Unlike other methods such as Finite Difference and Finite Element methods, the TLM method utilizes a physical discretization approach. In TLM, the field problem is replaced by an equivalent spatial network and the analogy between the fields and network quantities (voltage and current) is established. The equivalent network is then solved by iterative methods.

The outstanding features of the TLM method that make it particularly suitable for solving a wide range of electromagnetic field problems are

- 1) Great flexibility : The electromagnetic problem does not need to be formulated for every new structure.
- 2) Unconditional stability : Space and time steps are related by the propagation speed of the wave in the TLM mesh, which is a passive network and hence, unconditionally stable.
- 3) Observation of transient response to arbitrary excitation waveforms
- 4) Use of transmission line and network theory
- 5) Modeling of time-dependent materials and nonlinear devices
- 6) Visualization of the propagation of electromagnetic fields
- 7) Ease of programming

The FDTD method first introduced by Yee in 1966 [6], which solves Maxwell's equations numerically in the time domain on a spatial grid, is another popular numerical method. The TLM and FDTD methods are similar in several respects and complementary

[7][8][9] even though they are based on different modeling principles. These methods were combined to advantage for solving semiconductor problems [10].

However, the TLM method is different from FDTD in that the electric and magnetic fields are co-located. These advantages and unique characteristics of the TLM method brought us commercially available simulation tools such as Stripes and Mefisto [11].

1.2 Research Objectives

The 2D-TLM method has been used to model active nonlinear subregions of distributed circuits [12][13] where extra stubs were used for embedding lumped circuit devices into a TLM mesh. Regions of negative conductivity might cause spurious oscillations at the TLM mesh cut-off frequencies. To avoid this problem, the TLM mesh cut-off is chosen to be well above the active device cut-off frequency. A scheme to incorporate lumped voltage sources in 3D-TLM was presented in [14]. An embedding technique for linear passive elements was introduced in [15] where devices were directly connected to the TLM link lines.

The FDTD method has also been researched actively. A technique to embed elements into the 2D-FDTD grid, such as resistors, capacitors, inductors, diodes, and transistors, was proposed in [16]. A three-dimensional implementation with improvements was presented in [17]. A general scheme to incorporate lumped circuit elements into an FDTD grid by coupling SPICE (Simulation Program with Integrated Circuit Emphasis) with FDTD was described in [18] where the finite difference

formulation of Ampere's law has been directly represented by an equivalent circuit in the form of a SPICE input file.

The objective of this thesis is to develop several techniques for including lumped linear and nonlinear devices into a distributed system. Moreover, the final goal is to connect SPICE with the TLM algorithm to model more complex and extensive nonlinear circuits effectively.

1.3 Original Contributions

The above research objectives have been met by virtue of the following original contributions to the TLM method

- Star-type scheme to embed lumped circuit elements
 - Star-type implementation can be used as an alternative to node implementation in modeling linear and nonlinear passive and active devices in 2D- and 3D-TLM.
- Coupling SPICE with TLM
 - The connection between SPICE and TLM enables us to take full advantage of all existing device models in SPICE. Time consuming efforts such as derivation and programming of the discretized nonlinear equations describing the behavior of a device is avoided. The user can modify the SPICE input file without altering the TLM algorithm.

1.4 Preview of Contents

Chapter 2 covers the fundamental theory of the 2D- and 3D-TLM methods. The characteristics of TLM and sources of errors are discussed. Chapter 3 reviews the models

of nonlinear semiconductor devices such as $p-n$ junction diode and tunnel diode. This Chapter presents the I-V characteristic of the devices in a manner suitable for time domain discretization, and their operating principles.

Chapter 4 focuses on the three different device-embedding schemes, namely node, boundary, and star-type implementations. The schematic layouts of each technique and its properties are presented. Chapter 5 is devoted to validation of these schemes. Here, the discretized formulations for devices are derived, and the results obtained by each technique are compared and analyzed.

Chapter 6 focuses on a methodology to couple SPICE with the TLM algorithm. This algorithm is verified by comparing the results of SPICE with that of SPICE-TLM. The last Chapter ends this thesis with a discussion of future work and conclusion.

Chapter 2

The Transmission Line Matrix Method

2.1 Introduction

This chapter provides an overview of the fundamental theory of the 2D- and 3D-TLM methods. It also presents the characteristics of the TLM method and sources of errors. In order to solve a general electromagnetic problem, the computational region of interest must be discretized in time and space. A TLM mesh or network consists of orthogonal 1D transmission lines interconnected at nodes. The unit time step Δt is the time necessary for a wave to propagate from one node to an adjacent node. The mesh size Δl is the distance between two adjacent nodes. Therefore, the phase velocity (v_l) of the transmission line is

$$v_l = \frac{\Delta l}{\Delta t} \quad (\text{Eq 2.1})$$

In the TLM network, the propagation of electromagnetic fields can be described by the scattering process of the electrical quantities (voltages and currents) at each node. The correspondence between the electrical voltages and currents and the electromagnetic fields was first introduced in [19]. Analogous to the Huygen' principle [20], the TLM algorithm can be split into two steps (scattering and connection). In the scattering step, the impulses incident on a node are scattered isotropically in all four directions. Each scattered impulse carries one-fourth of the incident energy according to energy conservation. The scattering process in the TLM algorithm can be described by the following simple matrix equation

$$[{}_k V^r] = [S] \cdot [{}_k V^i] \quad (\text{Eq 2.2})$$

$[{}_k V^r]$: vector of reflected voltages at $t=k \Delta t$

$[{}_k V^i]$: vector of incident voltages at $t=k \Delta t$

$[S]$: impulse scattering matrix

In the connection step, the impulses emerging from a node become incident impulses on the neighboring nodes. This process can be described by

$$[{}_{k+1} V^i] = [C] \cdot [{}_k V^r] \quad (\text{Eq 2.3})$$

where $[C]$ denotes the connection matrix. The reflected impulses propagate to the neighboring nodes according to the connection matrix. The above process is described in Figure 2.1.

Many electromagnetic problems can be formulated as two-dimensional problems. For instance, the propagation of TE (Transverse Electric) and TM (Transverse Magnetic) modes in homogeneous parallel plate and rectangular waveguides involve only two spatial directions. The propagation of TE waves is thus described by the 2D-TLM shunt network, while the propagation of TM waves is represented by the 2D-TLM series network [21][22].

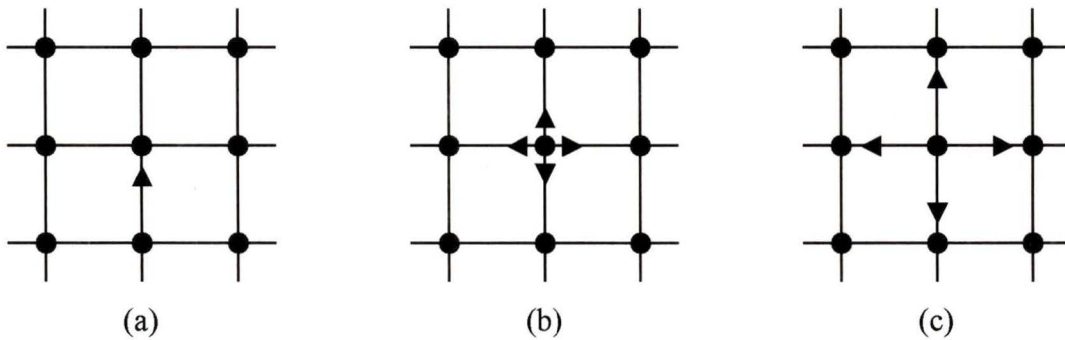


Figure 2.1 The description of the scattering and connection processes of the TLM algorithm. (a) Injection of impulse voltage (b) Scattering at the node (c) Connection to the neighboring nodes

When 2D-TLM is insufficient to solve electromagnetic problems, a three-dimensional TLM network must be employed. Of the 3D-TLM nodes developed for solving arbitrary structures, the SCN (Symmetrical Condensed Node) introduced by P. B. Johns is the most commonly used [23]. We will discuss the 2D-TLM shunt node and the symmetrical condensed node in the following subsections.

2.2 Shunt-Connected 2D-TLM Network

In order to model the propagation of a TE field in free space by the 2D-TLM network, the shunt nodes in Figure 2.2 (a) are employed. The lumped element equivalent circuit of the shunt node is shown in Figure 2.2 (b). Here, L denotes inductance per unit

length and C capacitance per unit length of the link lines. A cell is a square or rectangular subsection of the TLM mesh with a node at its center.

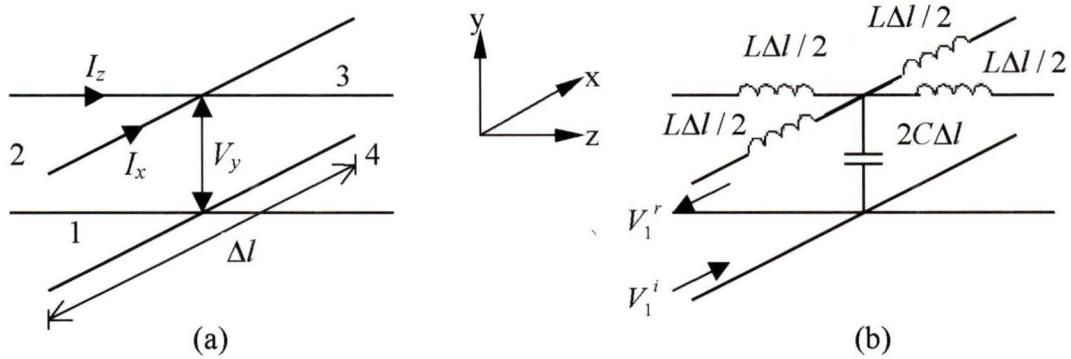


Figure 2.2 2D-TLM shunt node (a) TLM cell (b) its lumped element equivalent circuit

The propagation of a TE mode in dielectric lossy materials can be modeled by joining additional transmission lines to the nodes. In this case, the shunt node consists of the intersection of two transmission lines (link lines), an open-circuited transmission line stub of length $\frac{\Delta l}{2}$, and a matched transmission line. The inductance and capacitance of an open transmission line of length $\frac{\Delta l}{2}$ are $\frac{L}{y_s} \frac{\Delta l}{2}$ and $Cy_s \frac{\Delta l}{2}$, respectively: This open transmission line is called the permittivity stub [20]. y_s is the normalized characteristic admittance of the stub. The inductance and capacitance of a matched transmission line of length $\frac{\Delta l}{2}$ are $\frac{L}{g_s} \frac{\Delta l}{2}$ and $Cg_s \frac{\Delta l}{2}$, respectively. This matched transmission line is called the loss stub. g_s is the normalized shunt conductance. The permittivity stub is used to represent the property of the material filling the computation region, while the loss stub is employed to describe the loss of the material.

2.2.1 2D-TLM Shunt Node Wave Properties

If the mesh size $\Delta x = \Delta z = \Delta l$ is infinitesimally small, the 2D-TLM shunt node exactly describes the propagation of TE fields governed by Maxwell's equations. However, the fact that Δl is finite in practice causes errors. Therefore, in order to represent the propagation of the wave properly in space, the cell size Δl must be small compared with the wavelength of interest.

For the shunt node in Figure 2.2, the voltage and current changes in x - and z -direction are

$$\begin{aligned}\frac{\partial V_y}{\partial x} &= -L \frac{\partial I_x}{\partial t} \\ \frac{\partial V_y}{\partial z} &= -L \frac{\partial I_z}{\partial t} \\ \frac{\partial I_z}{\partial z} + \frac{\partial I_x}{\partial x} &= -2C(1 + \frac{y_0}{4}) \frac{\partial V_y}{\partial t} - \frac{g_0 \sqrt{\frac{C}{L}}}{\Delta x} V_y\end{aligned}\quad (\text{Eq 2.4})$$

The corresponding Maxwell's equations in a lossy medium obtained by setting

$\frac{\partial}{\partial y} = 0$ and $E_x = E_z = H_z = 0$, are

$$\begin{aligned}\frac{\partial E_y}{\partial x} &= -\mu_n \frac{\partial H_x}{\partial t} \\ \frac{\partial E_y}{\partial z} &= \mu_n \frac{\partial H_x}{\partial t} \\ \frac{\partial H_x}{\partial z} - \frac{\partial H_x}{\partial x} &= \epsilon_n \frac{\partial E_y}{\partial t} + \sigma_n E_y\end{aligned}\quad (\text{Eq 2.5})$$

where ε_n denotes the permittivity, μ_n the permeability, and σ_n the conductivity of the network.

The following correspondence between Eq (2.4) and (2.5) can be obtained.

$$\begin{aligned} Vy &\equiv Ey & Ix &\equiv Hz & Iz &\equiv -Hx \\ L &\equiv \mu_n & 2C(1 + \frac{y_0}{4}) &\equiv \varepsilon_n & \frac{g_0 \sqrt{\frac{C}{L}}}{\Delta x} &\equiv \sigma_n \end{aligned} \quad (\text{Eq 2.6})$$

If we assume that the nodes have no stub for modeling free space, the inductance and capacitance per unit length of the link lines are

$$\mu_0 = L \quad 2C = \varepsilon_0 \quad (\text{Eq 2.7})$$

and the wave equations are

$$\frac{\partial^2 Ey}{\partial x^2} + \frac{\partial^2 Ey}{\partial z^2} = \varepsilon_n \mu_n \frac{\partial^2 Ey}{\partial t^2} = \frac{1}{v_n^2} \frac{\partial^2 Ey}{\partial t^2} \quad (\text{Eq 2.8})$$

$$\frac{\partial^2 Vy}{\partial x^2} + \frac{\partial^2 Vy}{\partial z^2} = 2LC \frac{\partial^2 Vy}{\partial t^2} = \frac{1}{v_n^2} \frac{\partial^2 Vy}{\partial t^2} \quad (\text{Eq 2.9})$$

By comparing the wave equation (Eq 2.8) for the electric field and (Eq 2.9) for the voltage traveling in the TLM mesh, we can find the analogy between electromagnetic fields and electric quantities.

It can be seen from Eq (2.8) and Eq (2.9) that the velocity v_l and the characteristic impedance Z_l on the link lines are $\sqrt{2}$ times the velocity v_n of the voltage waves on the TLM network and the intrinsic impedance of the network, respectively.

2.2.2 2D-TLM Shunt Node Scattering matrix

A voltage impulse incident on a stub-loaded node is scattered into six transmission lines. The impulse scattered into the loss-stub is absorbed because this stub is terminated in a matched load. Five of these scattered impulses will be returned to the node. The reflection coefficient seen by an impulse incident on one of the four external ports of a node is

$$S_{ii} = \frac{2-y}{y} \quad i = 1 \dots 4 \quad (\text{Eq 2.10})$$

and the transmission coefficient is

$$S_{ki} = 1 + S_{ii} = \frac{2}{y} \quad k \neq i \quad (\text{Eq 2.11})$$

where $y=4+y_s+g_s$.

The reflection and transmission coefficients seen by the permittivity stub are

$$S_{55} = \frac{2y_s - y}{y} \quad S_{i5} = 1 + S_{55} = \frac{2y_s}{y} \quad (i \neq 5) \quad (\text{Eq 2.12})$$

Using Eq (2.10), (2.11) and (2.12), the scattering process is described by

$$\begin{matrix} \begin{bmatrix} V_1 \\ V_2 \\ V_3 \\ V_4 \\ V_5 \end{bmatrix}^r \\ \begin{matrix} \left[\right. \\ \left. \right]_k \end{matrix} \end{matrix} = \frac{1}{y} \begin{bmatrix} 2-y & 2 & 2 & 2 & 2y_s \\ 2 & 2-y & 2 & 2 & 2y_s \\ 2 & 2 & 2-y & 2 & 2y_s \\ 2 & 2 & 2 & 2-y & 2y_s \\ 2 & 2 & 2 & 2 & 2y_s - y \end{bmatrix} \begin{matrix} \begin{bmatrix} V_1 \\ V_2 \\ V_3 \\ V_4 \\ V_5 \end{bmatrix}^i \\ \begin{matrix} \left[\right. \\ \left. \right]_k \end{matrix} \end{matrix}$$

$$[S] = \frac{1}{y} \begin{bmatrix} 2-y & 2 & 2 & 2 & 2y_s \\ 2 & 2-y & 2 & 2 & 2y_s \\ 2 & 2 & 2-y & 2 & 2y_s \\ 2 & 2 & 2 & 2-y & 2y_s \\ 2 & 2 & 2 & 2 & 2y_s - y \end{bmatrix} \quad (\text{Eq 2.13})$$

where $[S]$ is the scattering matrix for a stub-loaded node.

The connection process can be represented by

$$\begin{aligned} {}_{k+1}V_1^i(x, z) &= {}_kV_3^r(x-1, z) & {}_{k+1}V_2^i(x, z) &= {}_kV_4^r(x, z-1) \\ {}_{k+1}V_3^i(x, z) &= {}_kV_1^r(x+1, z) & {}_{k+1}V_4^i(x, z) &= {}_kV_2^r(x, z+1) \\ {}_{k+1}V_5^i(x, z) &= {}_kV_5^r(x, z) & & \end{aligned} \quad (\text{Eq 2.14})$$

where the superscripts i and r denote incident and reflected impulse voltages, the subscripts k and $k+1$ represent the time in Δt .

The 2D series node is governed by a formulation, which is dual to that of the shunt node. More details on the properties of the 2D-TLM series node can be found in [20][21][22].

2.3 The 3D-TLM Network

The modeling of electromagnetic problems that cannot be formulated as two-dimensional problems requires the three-dimensional TLM cell with six field components. Unlike FDTD [24] and the expanded node for the 3D-TLM [25], in which the positions of the electric and magnetic field components are staggered in space, the symmetrical condensed node for the 3D-TLM [23], which is the most commonly used, defines all electric and magnetic field components at the same point in space. Its main

advantage is that it allows us to implement boundary conditions in a simple manner since both E and H are defined in the boundaries of each cell.

Figure 2.3 shows the structure of the symmetric condensed node. It consists of 12 ports representing 2 polarizations in each direction. The impulse voltages are carried on transmission lines represented by thick lines. Two orthogonal transmission lines such as 7 and 12 do not directly couple with each other.

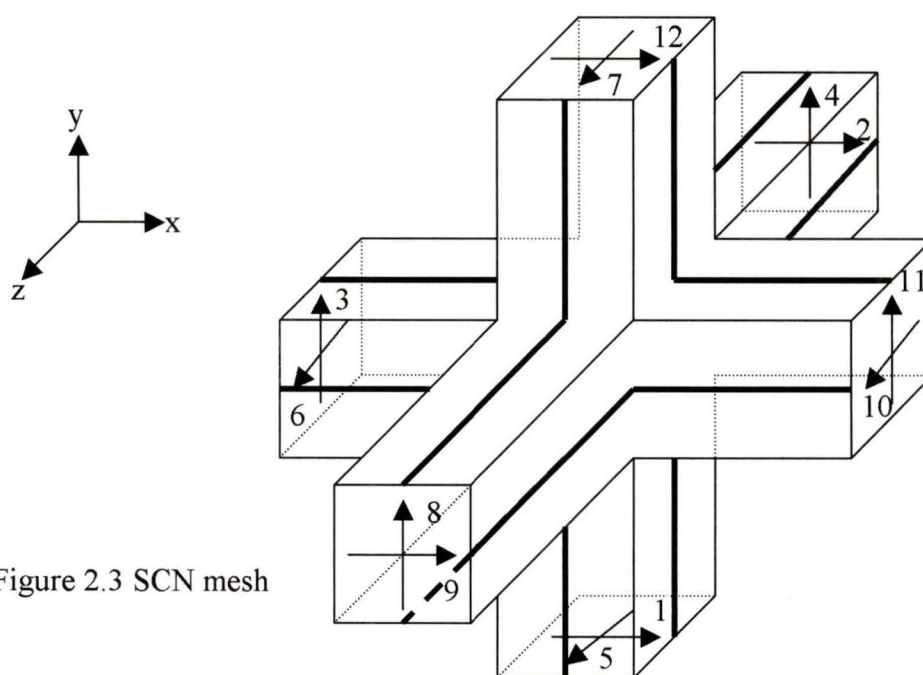


Figure 2.3 SCN mesh

The scattering properties are obtained from general energy and charge conservation principles as described in [21] and [23]. The scattering matrix $[S]$ (Eq 2.15) relating reflected ${}_k V^r$ to incident ${}_k V^i$ voltages is a 12×12 matrix.

$$[S] = 0.5 \begin{bmatrix} 0 & 1 & 1 & 0 & 0 & 0 & 0 & 0 & 1 & 0 & -1 & 0 \\ 1 & 0 & 0 & 0 & 0 & 1 & 0 & 0 & 0 & -1 & 0 & 1 \\ 1 & 0 & 0 & 1 & 0 & 0 & 0 & 1 & 0 & 0 & 0 & -1 \\ 0 & 0 & 1 & 0 & 1 & 0 & -1 & 0 & 0 & 0 & 1 & 0 \\ 0 & 0 & 0 & 1 & 0 & 1 & 0 & -1 & 0 & 1 & 0 & 0 \\ 0 & 1 & 0 & 0 & 1 & 0 & 1 & 0 & -1 & 0 & 0 & 0 \\ 0 & 0 & 0 & -1 & 0 & 1 & 0 & 1 & 0 & 1 & 0 & 0 \\ 0 & 0 & 1 & 0 & -1 & 0 & 1 & 0 & 0 & 0 & 1 & 0 \\ 1 & 0 & 0 & 0 & 0 & -1 & 0 & 0 & 0 & 1 & 0 & 1 \\ 0 & -1 & 0 & 0 & 1 & 0 & 1 & 0 & 1 & 0 & 0 & 0 \\ -1 & 0 & 0 & 1 & 0 & 0 & 0 & 1 & 0 & 0 & 0 & 1 \\ 0 & 1 & -1 & 0 & 0 & 0 & 0 & 0 & 1 & 0 & 1 & 0 \end{bmatrix} \quad (\text{Eq 2.15})$$

Let us consider the propagation process in a regular SCN mesh by studying the scattering matrix. Exciting port 8 on all the nodes on a x - y plane in order to propagate in the z - direction will produce the following scattered impulse voltages.

$${}_k V_3^r = -{}_k V_5^r = {}_k V_7^r = -{}_k V_{11}^r = 0.5 \quad (\text{Eq 2.16})$$

At the next time step, the incident voltages on node (x,y,z) come from neighboring nodes. i.e.,

$${}_{k+1} V_3^i(x, y, z) = {}_k V_{11}^r(x-1, y, z) = 0.5$$

$${}_{k+1} V_5^i(x, y, z) = {}_k V_7^r(x, y-1, z) = 0.5$$

$${}_{k+1} V_7^i(x, y, z) = {}_k V_5^r(x, y+1, z) = -0.5$$

$${}_{k+1} V_{11}^i(x, y, z) = {}_k V_3^r(x+1, y, z) = 0.5 \quad (\text{Eq 2.17})$$

The voltages incident upon node (x,y,z) produce the only reflected voltage ${}_{k+1} V_4^r$, which is equal to 1. It can be easily seen from this fact that it takes two time-steps to

propagate the distance Δl without dispersion. Therefore, the time discretization must be such that

$$\Delta t = \frac{\Delta l}{2v} \quad (\text{Eq 2.18})$$

where v is the medium propagation velocity.

At each node of the TLM network the electric and magnetic fields can be calculated from the incident voltages on the link lines. The relationship is given in Eq (2.19). Similar expressions apply for other electric and magnetic field components.

$$E_x = -\frac{V_1^i + V_2^i + V_9^i + V_{12}^i}{2\Delta x}$$

$$H_x = \frac{V_4^i - V_5^i + V_7^i - V_8^i}{2Z_l \Delta x} \quad (\text{Eq 2.19})$$

where Z_l is the characteristic impedance of the transmission lines (link lines).

In SCN 3D-TLM, as in the 2D-TLM shunt and series nodes, capacitive and inductive stubs can be connected to the node in order to allow for variations in ϵ , μ , node shape, and dimensions.

The connection of stubs does not affect the connection process, but affects the scattering matrix (Eq 2.20). Three capacitive (open) and inductive (short) stubs produce the 18×18 scattering matrix [23] as given in Eq 2.20.

	1	2	3	4	5	6	7	8	9	10	11	12	13	14	15	16	17	18
[S]=	a	b	d						b		-d	c	g					i
	b	a				d			c	-d		b	g				-i	
	d		a	b				b			c	-d		g				-i
			b	a	d		-d	c			b			g		i		
				d	a	b	c	-d		b					g	-i		
		d			b	a	b		-d	c					g		i	
				-d	c	d	a	d		b					g	i		
			b	c	-d		d	a		b				g		-i		
	b	c				-d			a	d		b	g				i	
		-d			b	c	b		d	a					g		-i	
	-d		c	b				b			a	d		g				-i
	c	b	-d						b		d	a	g					-i
	e	e							e			e	h					
			e	e				e			e			h				
				f	-f		f	-f								j		
		-f				f			f	-f							j	
	f		-f								f	-f						j

(Eq 2.20)

The coefficients of the scattering matrix in Eq 2.20 are

$$a = -\frac{\hat{Y}}{2(4+\hat{Y})} + \frac{\hat{Z}}{2(4+\hat{Z})} \quad b = \frac{2}{(4+\hat{Y})}$$

$$c = -\frac{\hat{Y}}{2(4+\hat{Y})} - \frac{\hat{Z}}{2(4+\hat{Z})} \quad d = \frac{2}{(4+\hat{Z})}$$

$$e = b \quad f = \hat{Z}d \quad g = \hat{Y}b$$

$$h = \frac{\hat{Y} - 4}{4 + \hat{Y}} \quad i = d \quad j = \frac{4 - \hat{Z}}{4 + \hat{Z}} \quad (\text{Eq 2.21})$$

The values of \hat{Y} and \hat{Z} used in these expressions are chosen to correspond to the relevant stubs. If the cubic cells are used for modeling an isotropic medium, then all the admittances and impedances are

$$\hat{Y} = \hat{Y}_x = \hat{Y}_y = \hat{Y}_z = 4(\varepsilon_r - 1)$$

$$\hat{Z} = \hat{Z}_x = \hat{Z}_y = \hat{Z}_z = 4(\mu_r - 1) \quad (\text{Eq 2. 22})$$

In order to deal with general inhomogeneous anisotropic media and to use a graded mesh, which is employed to save on computer requirements by using a fine mesh only in areas of rapid field variation, three different admittances and impedances must be taken into account in the determination of the scattering matrix. The general expressions are given by

$$\hat{Y}_x = \frac{2\varepsilon_r}{u_0\Delta t} \frac{\Delta y\Delta z}{\Delta x} - 4 \quad \hat{Y}_y = \frac{2\varepsilon_r}{u_0\Delta t} \frac{\Delta x\Delta z}{\Delta y} - 4 \quad \hat{Y}_z = \frac{2\varepsilon_r}{u_0\Delta t} \frac{\Delta x\Delta y}{\Delta z} - 4$$

$$\hat{Z}_x = \frac{2\mu_r}{u_0\Delta t} \frac{\Delta y\Delta z}{\Delta x} - 4 \quad \hat{Z}_y = \frac{2\mu_r}{u_0\Delta t} \frac{\Delta x\Delta z}{\Delta y} - 4 \quad \hat{Z}_z = \frac{2\mu_r}{u_0\Delta t} \frac{\Delta x\Delta y}{\Delta z} - 4$$

$$(\text{Eq 2. 23})$$

where $u_0 = \frac{1}{\sqrt{\varepsilon_0\mu_0}}$.

The relationship between the electric and magnetic fields and the voltages are given by

$$E_x = -\frac{2(V_1^i + V_2^i + V_9^i + V_{12}^i + \hat{Y}_x V_{13}^i)}{\Delta x(4 + \hat{Y}_x)}$$

$$H_x = \frac{2(V_4^i - V_5^i + V_7^i - V_8^i - V_{16}^i)}{\Delta x(4Z_0 + Z_0 Z_z)} \quad (\text{Eq 2.24})$$

Similar expressions apply for other electric and magnetic field components. More details about the 3D-TLM node can be found in [21][23].

2.4 Characteristics of the TLM method and Sources of Errors

2.4.1 Characteristics of the TLM method

The 2D-TLM series and shunt nodes and the symmetrical condensed node for 3D-TLM are different from FDTD or the expanded node for the 3D-TLM in that the electric and magnetic field components can be defined at the same point in space. This allows us to define boundary conditions in a simple manner.

Just like the FDTD method, the TLM process is also reversible in time. This is possible because the scattering matrix of the TLM process is invertible. During the time reversal, scattering and connection are performed in reverse sequence.

2.4.2 Sources of Errors

The accuracy of TLM results is limited by three kinds of errors (velocity error, coarseness error, and truncation error), which will be discussed below.

1) Velocity Error

If the wavelength λ of a signal in the TLM network is much larger than mesh size Δl , its phase velocity in the TLM network is virtually independent of the direction of propagation. However, as the wavelength of the signal decreases, the wave velocity becomes dispersive and depends on the direction of propagation and on frequency. This is known as velocity error. Velocity error can be reduced by using a fine TLM mesh such

that $\frac{\Delta l}{\lambda} \leq 0.1$. This fine mesh should be compatible with the computer memory resources. More details about the dispersion characteristic of 2D- and 3D-TLM can be found in [26][27].

2) Coarseness Error

Coarseness error occurs when the TLM mesh is too coarse to resolve highly non-uniform fields (field singularities) at sharp corners. This error is dominant when analyzing structures with thin metallic strips and sharp corners. Even though the mesh size is sufficiently small everywhere else in the structure, it is too large to resolve the high spatial harmonics at singularities. One way to reduce this error is to use a very fine mesh in the whole computational region. This would require very large memory and CPU time. A better way to reduce this error is to introduce a graded mesh to provide higher resolution in the non-uniform field region only. This approach, however, requires more complicated discretization techniques and reduces the length of the time step. Another method is to locally embed a finer mesh into the coarse mesh [24]. Even though this avoids the reduction of the time step, it creates interfacing problems between the fine and coarse regions. This approach must conserve charge and energy, and must not introduce parasitic reflections and delays.

3) Truncation Error

We must truncate the computation in time to analyze the response. This leads to the so-called truncation error. Due to the finite duration of the time domain response, the frequency domain response will be given by the convolution of the desired frequency

spectrum with a $\frac{\sin x}{x}$ function, giving rise to the Gibbs' phenomenon. In other words, its Fourier transform is not a line spectrum, but rather a superposition of sinc functions, which may interfere with each other such that the spectral peaks are slightly shifted. In order to get the desired frequency spectrum, the $\frac{\sin x}{x}$ function must be as narrow as possible. Satisfactory results can be obtained by using sufficient computation time, or by using specific windows in the Fourier transform.

2.5 Conclusion

In this chapter, the basic theory and algorithms of the 2D-and 3D-TLM has been summarized. The principal characteristics of the TLM method have been discussed. In addition, the sources of errors encountered in the resolution of electromagnetic problems and their correction methods have been reviewed.

Chapter 3

Review of Non-Linear Device Characteristics and their Circuit Models

3.1 Introduction

This chapter gives an overview of the characteristics of nonlinear semiconductor devices to be embedded in the TLM mesh. Time domain numerical methods such as FDTD and TLM are suitable for large signal or transient analysis of circuits containing such devices. Many kinds of devices such as diodes, BJT (Bipolar Junction Transistor), JFET (junction Field-Effect Transistor) and MOS (Metal Oxide Semiconductor) transistor have been studied in the past years, and therefore the equivalent circuits of the devices, including package and thermal effects and noise, have been established and can be used to connect the devices into the TLM mesh. These equivalent circuit models are useful for the design of integrated circuits, and have been incorporated in SPICE.

In this chapter, the basic characteristics of p - n junction and tunnel diodes and an ideal bipolar transistor are reviewed, and the equivalent circuit models used in SPICE for those devices are discussed. Note that we must represent these devices by their nonlinear differential or integral equations in time domain in order to predict their interaction with the electromagnetic fields.

3.2 P - N Junction Diode

The p - n junction diode is the simplest nonlinear semiconductor made by joining a n -type material to p -type material. Eq (3.1) represents the I-V characteristic of the diode.

$$i_d = I_s \left[\exp\left(\frac{qv_d}{nkT}\right) - 1 \right] \quad (\text{Eq 3.1})$$

where i_d = current in the diode
 v_d = potential difference across the diode
 I_s = leakage current
 q = electron charge : 1.6×10^{-19} (C)
 k = Boltzmann's constant: 1.38×10^{-23} J/°K
 T = absolute temperature in degrees Kelvin
 n = empirical constant between 1 and 2

In order to obtain a large-signal diode model, the charge-storage effects of the device should be taken into account [28]. Charge storage results from excess minority carriers injected across the junction in forward bias mode. This charge (Eq 3.2) is proportional to the total current injected into the junction. These effects can be represented by a diffusion capacitance C_d (Eq. 3.3).

$$Q_d = \tau_d i_d(v_d) \quad (\text{Eq 3.2})$$

where τ_d (transit time of the diode) denotes the minimum time required to either store or remove the charge.

$$C_d(v_d) = \frac{dQ_d}{dv_d} = \frac{q}{kT} \tau_d I_s \exp\left(\frac{qv_d}{kT}\right) \quad (\text{Eq 3.3})$$

The presence of a dipole consisting of fixed positive and negative charges in the depletion region leads to a junction capacitance C_j (Eq 3.4) that is dominant during reverse and small forward bias. Since the number of charges that exist in the depletion region varies with the applied voltage V_d , the value of C_j depends on V_d .

$$C_j(v_d) = \frac{C_j(0)}{\sqrt{1 - \frac{v_d}{\phi_0}}} \quad \text{for} \quad v_d < 0.5 \cdot \phi_0$$

$$C_j(v_d) = \frac{C_j(0)}{0.5^{1.5}} \left(0.25 + \frac{v_d}{2\phi_0}\right) \quad \text{for} \quad v_d \geq 0.5 \cdot \phi_0 \quad (\text{Eq 3.4})$$

where $C_j(0)$ is the zero-bias junction capacitance and ϕ_0 is the built-in voltage [28].

3.3 Tunnel Diode

The tunnel diode is a p - n junction diode with a dynamic negative resistance. The negative resistance exists due to the tunnel effect of electrons in the p - n junction. Tunnel diodes are used in microwave amplifiers, microwave oscillators, and binary memory because of their low cost, light weigh, high speed, low-power operation, low noise, and high peak-current to valley-current ratio.

Current flow in a tunnel diode is due to three distinct effects [29]: thermal current which is analogous to that in a conventional diode, tunnel current due to the direct tunneling effect, and excess current due to the indirect tunneling effect. Writing these three terms in PSpice's extended syntax, we get the following:

$$I = I_v \cdot \exp(V - V_v) + \frac{I_p \cdot V}{V_p} \exp\left(1 - \frac{V}{V_p}\right) + I_p \cdot \exp\left(-\frac{V_{fp}}{V_{tl}}\right) \cdot \exp\left(\frac{V}{V_{tl}} - 1\right) \quad (\text{Eq 3.5})$$

where a thermal voltage $V_{tl} = kT/q = 25.86\text{mV}$ at $T = 300\text{K}$.

Figure 3.1 shows the I - V characteristics of a tunnel diode. The main characteristics of a tunnel diode I - V curve are the peak voltage V_p and current I_p , the valley voltage V_v and current I_v , and the forward peak voltage V_{fp} . The tunnel current decreases in the voltage region $V_p < V < V_v$, but this current increases exponentially for $V > V_v$ like the conventional p - n junction diode current.

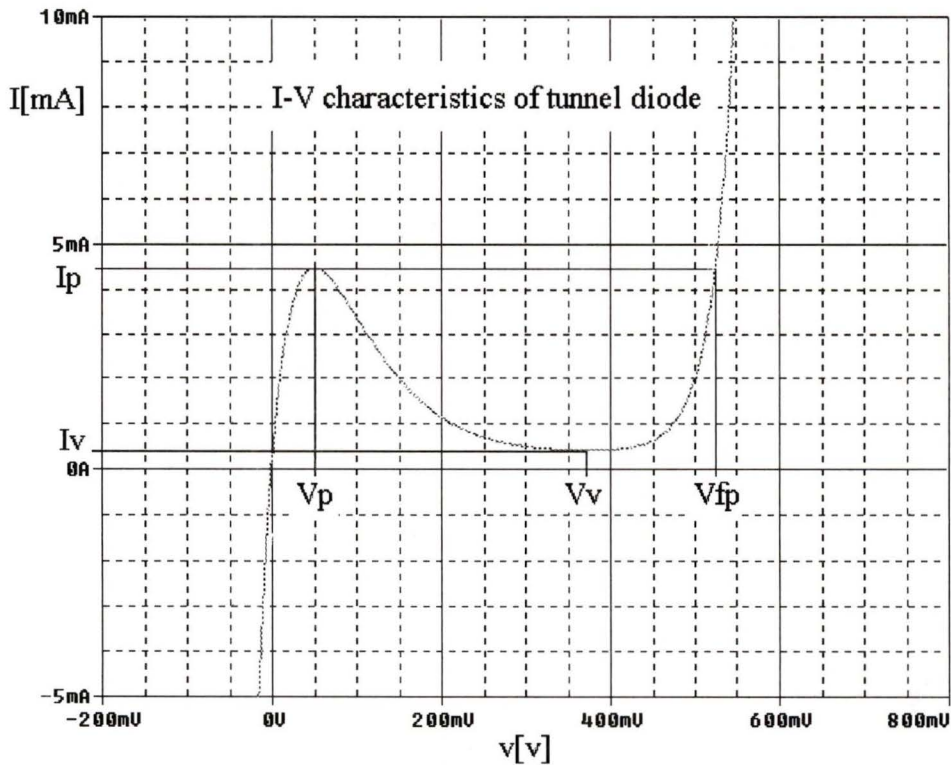


Figure 3.1 I - V characteristics of tunnel diode

3.4 Bipolar Junction Transistor

In this section, the I - V characteristic of a NPN bipolar junction transistor is reviewed. The Ebers-Moll model of the ideal BJT in Figure 3.2 is characterized by the saturation current (I_s), the ideal maximum forward current gain (β_f), and the ideal maximum reverse current gain (β_r).

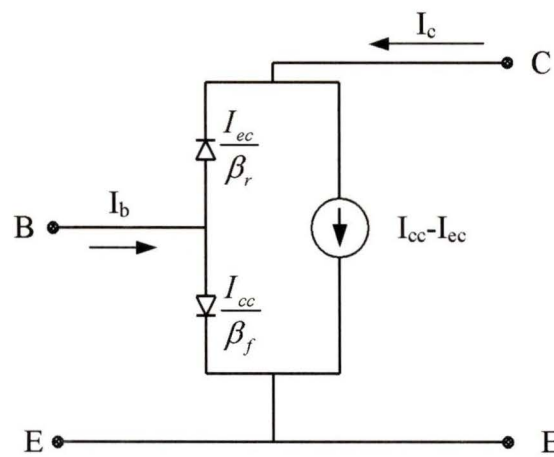


Figure 3.2 Ebers-Moll large-signal model of a Bipolar Junction Transistor

The BJT's terminal currents are given by

$$\begin{aligned}
 I_c &= I_s \left(e^{\frac{qV_{be}}{kT}} - e^{\frac{qV_{bc}}{kT}} \right) - \frac{I_s}{\beta_r} \left(e^{\frac{qV_{bc}}{kT}} - 1 \right) \\
 I_b &= \frac{I_s}{\beta_f} \left(e^{\frac{qV_{be}}{kT}} - 1 \right) + \frac{I_s}{\beta_r} \left(e^{\frac{qV_{bc}}{kT}} - 1 \right)
 \end{aligned}
 \tag{Eq. 3.6}$$

This ideal BJT model neglects many nonlinear parameters which must be taken into account for a practical BJT. In practice, it is difficult to include all BJT parameters in a TLM simulation since it is not straightforward to solve the extensive coupled nonlinear

equations. However, SPICE provides a well-established BJT model. Therefore, we preferred to embed a BJT into the TLM network using a SPICE program rather than discretizing and programming the nonlinear equations directly.

3.5 Conclusion

This chapter covered some basic characteristics of nonlinear semiconductor devices and the derivation of the equivalent circuit models for those devices. These equivalent circuits are suitable for embedding into the TLM mesh using different device embedding techniques. More equivalent models for other semiconductor devices such as JFET and MESFET transistors are available in the literature [28] and can also be incorporated in the TLM algorithm in a similar manner.

Chapter 4

Lumped and Distributed Device Embedding Techniques

4.1 Introduction

The TLM method has the advantage that electromagnetic field equations are modeled by means of transmission line networks [23]. Therefore, embedding of lumped and distributed devices in the TLM mesh is straightforward since the equivalent circuits of those devices can be connected to the nodes using transmission lines. However, due to the discrete nature of TLM, the behavior of an embedded device will depend on its numerical implementation.

In the FDTD method [16], the lumped device is embedded into a cell by extending Maxwell's equations (Ampere's law). A forward time average for the E term in the current density is taken to avoid instability in the FDTD method.

There exist several techniques for embedding devices into the TLM network. In this Chapter we discuss three different embedding techniques. Figure 4.1 shows the

simple embedding schematics for node (a) and (c), cell-boundary (b) and (d), and star-type (e) implementations.

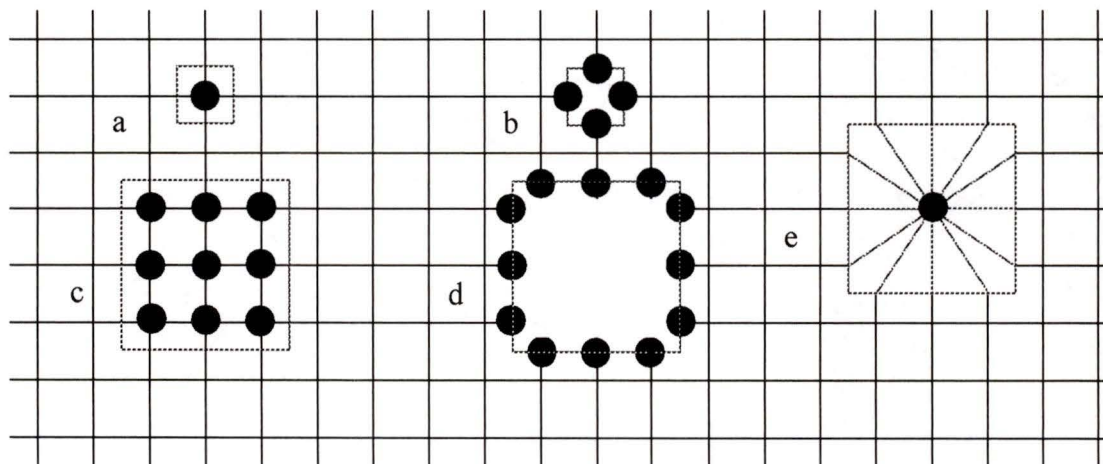


Figure 4.1 Typical node and boundary implementations of lumped devices in a TLM mesh. (a) Single Node implementation (b) 1x1 boundary implementation (c) 3x3 node implementation (d) 3x3 boundary implementation (e) 3x3 Star-type implementation. The mesh size is the same ($\Delta l=1\text{mm}$) in all cases. The 50Ω parallel plate waveguide is $31 \Delta l$ wide.

In many cases, the device may occupy a volume that exceeds the size of a single cell, yet the dimensions of this volume remain small compared to the wavelength. We are thus faced with a situation where the device is distributed over several TLM cells but remains quasi-lumped from a field perspective. The question thus arises how the device will interact with the field in such a situation. The effect of device connection and spreading over a number of nodes is better explained through an example. We consider a 50Ω resistor placed in a matched 50Ω parallel plate waveguide and compute the S-parameters. The width of the waveguide is discretized finely into 31 cells of size $\Delta l=1\text{mm}$. The resistor is connected to 1 and 9 nodes in a manner shown in Figure 4.1, using both node and cell-boundary connections. In all cases, the volume occupied by the

element remains small compared with the wavelength in the frequency range from 0 to 6 GHz.

Figure 4.2 shows the equivalent circuit for calculating the theoretical S-parameters of an ideal 50Ω resistor. These parameters can be obtained using transmission line theory or by converting the ABCD matrix of the circuit into S-Parameters. The reflection coefficient seen at port 1 when port 2 is terminated in a matched load of 50Ω is $-1/3$. Therefore, the transmission coefficient is $1-1/3=2/3$.

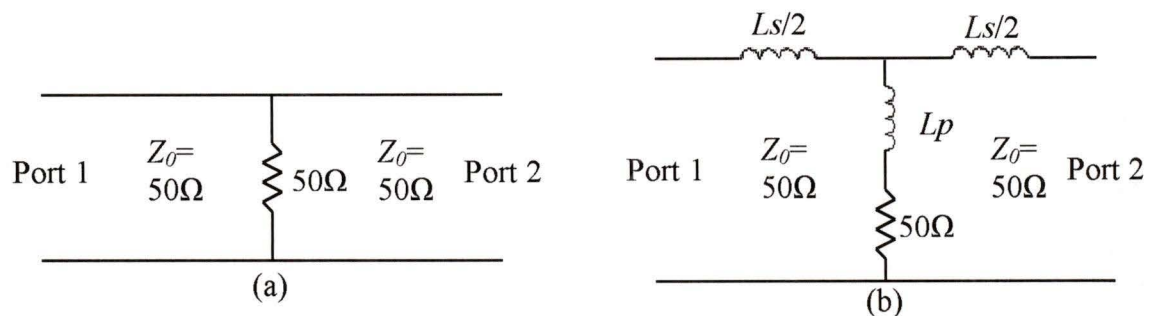


Figure 4.2 (a) The ideal equivalent circuit of a 50Ω resistance in a transmission line (b) Equivalent circuit of a 50Ω resistive post in a parallel plate waveguide with 50Ω characteristic impedance, including parasitic reactances.

Figure 4.3 compares the S-parameters obtained with the different embedding techniques. At very low frequencies, the effect of the reactive parasitic elements disappears, and all device implementations converge to the theoretical values of $|S_{11}|=1/3$ and $|S_{21}|=2/3$ of the ideal equivalent circuit in Fig. 4.2 (a). However, at higher frequencies, the effect of the finite size of the device due to its parasitic reactances becomes more pronounced, underlining the importance of spatial distribution of the equivalent elements.

As long as the geometrical size of the device remains small compared to the wavelength, a relatively coarse discretization of the device volume is sufficient for its

accurate modeling, including its parasitic elements. For example, if we refine the discretization of the 50Ω device in Figure 4.2 by a factor of 8 (from $\Delta l=2\text{mm}$ to $\Delta l=0.25\text{mm}$) while keeping the absolute dimensions the same, the difference in S-Parameters is only 0.01%. Node and boundary implementations also yield different responses even when the same physical volume is used. This is because the boundary model excludes the electromagnetic field completely from the volume it occupies.

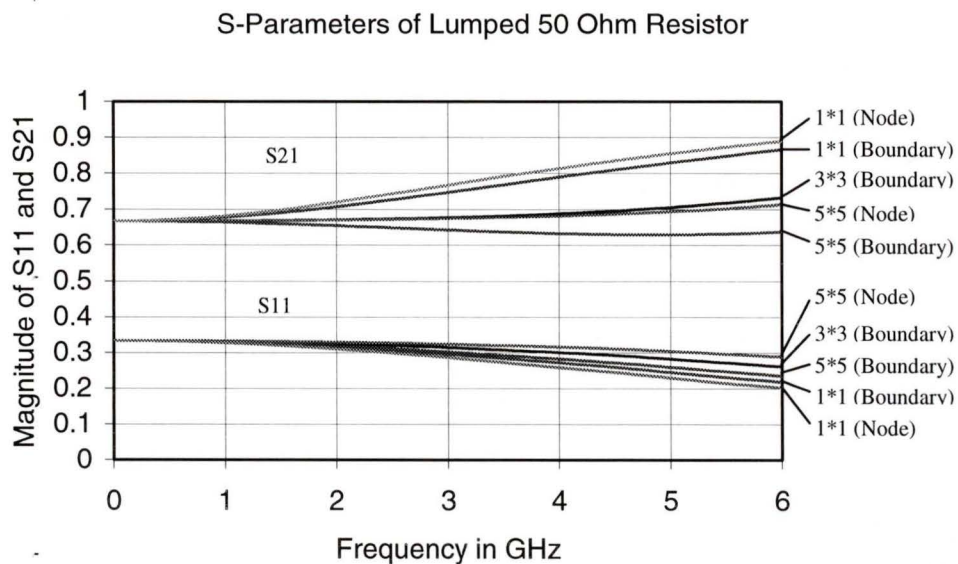


Figure 4.3 S-Parameters of a lumped 50 Ohm resistor placed in a matched 50 Ohm parallel plate waveguide computed with TLM using different implementations outlined in Figure 4.1

The situation becomes more complex when nonlinear and, in particular, active elements are embedded. From a physical point of view, it would be more realistic to spread the device over a finite volume corresponding to its physical size. However, if this results in the division of the equivalent circuit into several parallel devices, two types of problems may arise. Separate sub-devices are created which may interact in a parasitic fashion that is non-physical, involving the local resonant properties of the discrete mesh.

In the presence of gain, this may lead to instabilities due to the excitation of spurious oscillations. Also, the nonlinear differential equations governing the device must be solved separately for each sub-device, leading to increased computational demands.

In the following subsection, the three different embedding techniques are discussed in detail.

4.2 Node Implementation

The node implementation used to connect lumped elements to the TLM mesh is the same as the method introduced in [12][13]. In general, a device can be directly connected to either the TLM node or the link lines of the TLM mesh [30]. It can also be connected to the TLM node through a stub of length $\Delta/2$ [12].

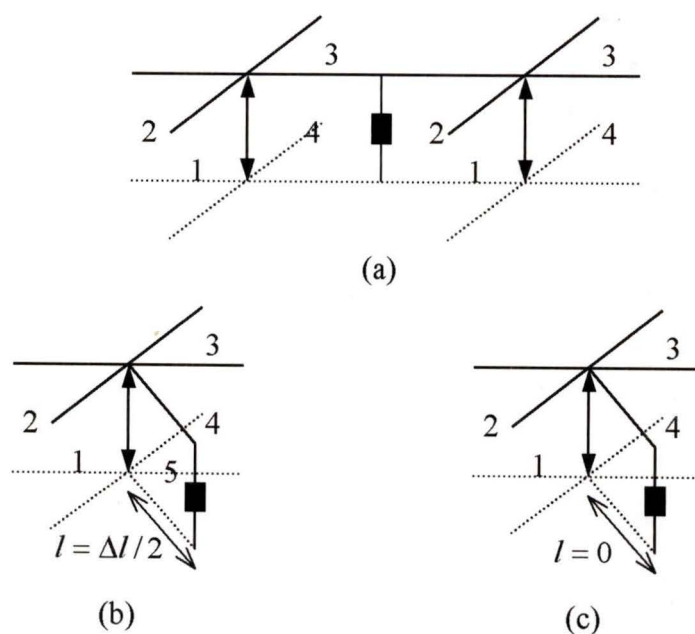


Figure 4.4 Models for connecting lumped elements to a TLM network: (a) link-line connection, (b) node connection with device stub of length $\Delta/2$ and (c) node connection with device stub of zero length. The TLM link lines are numbered 1 - 5.

The first approach (a) in Figure 4.4 requires the modification of the connection matrix at each time step. In this approach, the reflected voltages from a device travel toward the node and some of them will be reflected back into the device. This reflection causes a coupling between the linear and nonlinear part of the circuit [12][13]. However, this coupling does not affect the value of the simulation results. The second approach (b) employs a stub of length $\Delta l / 2$ to ensure synchronism of the impulses in the TLM mesh. In this method, the scattering matrix is modified by the device stub, but is not changed at each time step.

The main advantage of node implementation is that the decoupling of the linear and nonlinear parts of the circuit can be achieved by choosing the appropriate admittance value of the device stub. The disadvantage of this approach is that the device stub introduces an extra reactance in the equivalent circuit of the device. However, such extra reactance can be eliminated by reducing the length of the device stub to zero (c). The only difference between the approaches (b) and (c) is that (c) introduces no time delay.

4.2.1 The embedding of a one-port lumped device in 2D-TLM

In the following, the modeling of a one-port lumped device in 2D-TLM will be examined. The total voltage in Figure 4.5 across the lumped circuit and the current flowing toward it at time $k\Delta t$ are given by

$$\begin{aligned} {}_kV &= {}_kV_s^r + {}_kV_s^i \\ {}_kI &= Y_s \{ {}_kV_s^r - {}_kV_s^i \} \end{aligned} \quad (\text{Eq 4.1})$$

where Y_s is the characteristic admittance of the device stub.

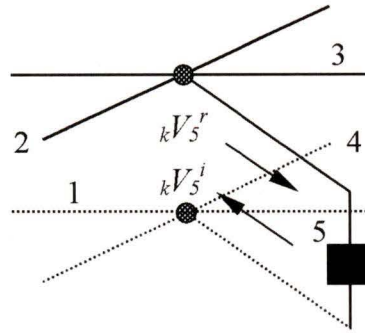


Figure 4.5 A lumped device connected in parallel to a 2D-TLM shunt node

The general current-voltage equations describing the lumped circuit can be expressed as

$$i(t) = f\left\{v(t), \frac{dv(t)}{dt}, \frac{d^2v(t)}{dt^2}, \dots\right\} \quad (\text{Eq 4.2})$$

This can be rewritten in discrete form by using a central difference scheme at the half time step $(k - 1/2)\Delta t$ to give

$$\begin{aligned} \frac{dV}{dt} \text{ at } k-1/2 &= \frac{{}^k V - {}^{k-1} V}{\Delta t} \\ \frac{dI}{dt} \text{ at } k-1/2 &= \frac{{}^k I - {}^{k-1} I}{\Delta t} \\ V(t) \text{ at } k-1/2 &= \frac{{}^k V + {}^{k-1} V}{2} \\ I(t) \text{ at } k-1/2 &= \frac{{}^k I + {}^{k-1} I}{2} \end{aligned} \quad (\text{Eq 4.3})$$

The unknown impulse ${}^k V_5^i$ can be obtained by substituting Eq 4.1 and 4.3 into Eq 4.2. Therefore, the voltage incident upon the node from the device has the form

$${}^k V_5^i = f({}^k V_5^r, {}^{k-1} V_5^r, {}^{k-2} V_5^r, \dots) \quad (\text{Eq 4.4})$$

Let us consider the situation where the device volume exceeds the size of a single TLM cell. In this case, it is very important to know how many cells are occupied by the device volume in the direction of the feeding voltage or in its perpendicular plane. Figure 4.6 shows the volume of the device occupying more than a single TLM cell. The device volume consists of H identical equivalent sub-devices in the direction of the feeding voltage V_y and W sub-devices in the plane perpendicular to its direction. The lumped device is thus modeled as a series combination of identical equivalent sub-devices in the direction of the feeding voltage. It can also be viewed as a parallel combination of identical equivalent sub-devices in the perpendicular plane.

In order to model the devices properly, the impedance values of the identical equivalent circuits are multiplied by W/H . Also, the admittance values are multiplied by H/W . The current source values must be divided by W , while the voltage source must be divided by H . Hence, each sub-device acts according to only the local field at the corresponding TLM cell.

Instabilities may, however, arise in modeling nonlinear active devices such as Tunnel or Gunn diodes if several active sub-devices are connected in series. Extra computational efforts to solve $H \times W$ nonlinear equations describing the behavior of a nonlinear device at each time step are required.

An embedding technique for nonlinear active devices was introduced in [31]. In this technique, only a single device occupies the whole active region in the direction of the feeding voltage. Such a device consists only of parallel sub-devices as shown in Figure 4.7.

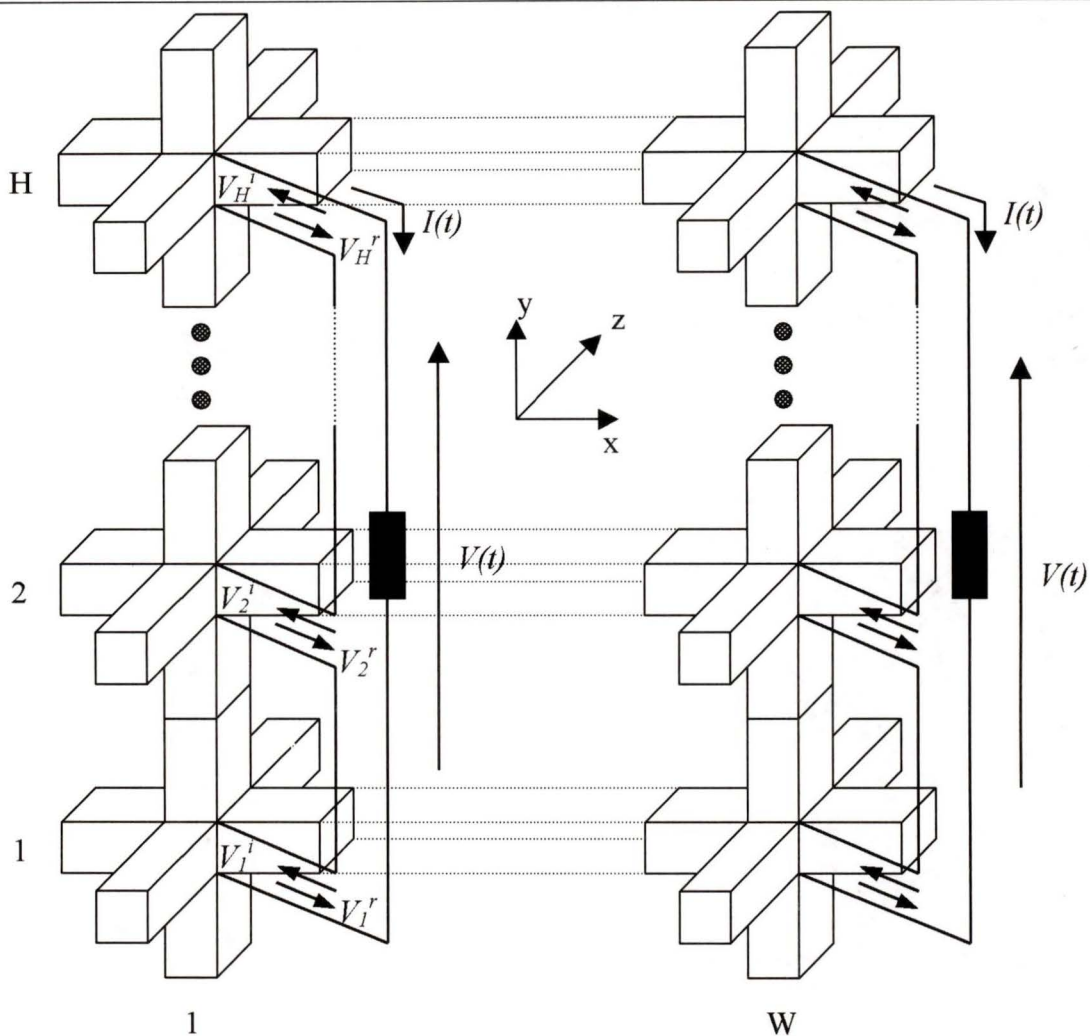


Figure 4.7 A single element connected to a 3D-TLM mesh by means of stacked stubs in the direction of the feeding voltage (V_y)

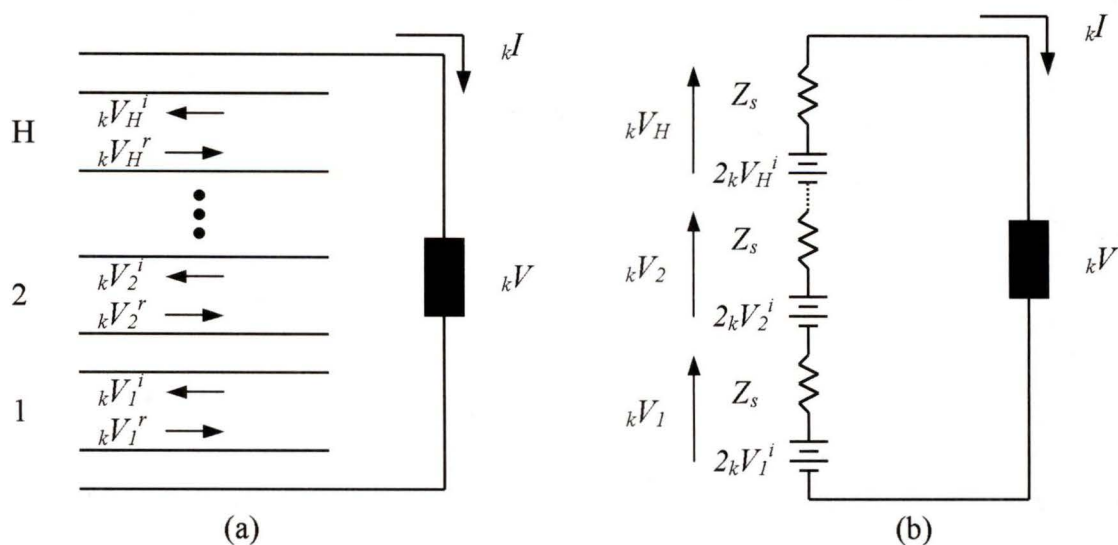


Figure 4.8 The stacked stub arrangement (a) and its Thevenin equivalent circuit (b). Z_s is the characteristic impedance of the stubs.

Considering the Thevenin equivalent circuit of each active region in Figure 4.8,

Eq 4.1 can be rewritten as

$${}_kV = {}_kV_1 + {}_kV_2 + \cdots + {}_kV_H = \sum_{h=1}^H {}_kV_h = \sum_{h=1}^H [{}_kV_h^r + {}_kV_h^i] \quad (\text{Eq 4.5.a})$$

$$\begin{aligned} {}_kI &= \frac{1}{H} Y_s [{}_kV - 2({}_kV_1^i + {}_kV_2^i + \cdots + {}_kV_H^i)] \\ &= \frac{1}{H} Y_s ({}_kV_1^r - {}_kV_1^i + {}_kV_2^r - {}_kV_2^i + \cdots + {}_kV_H^r - {}_kV_H^i) \end{aligned} \quad (\text{Eq 4.5.b})$$

where H is the number of TLM cells occupied by sub-device in the direction of the feeding voltage, and each cell is numbered by h . Y_s is the characteristic admittance of the device stub. Note that the total characteristic impedance of the stacked stub is HZ_s .

The amount of current flowing in each stub is the same so that

$${}_kV_1^r - {}_kV_1^i = {}_kV_2^r - {}_kV_2^i = \cdots = {}_kV_H^r - {}_kV_H^i \quad (\text{Eq 4.5.c})$$

Therefore, Eq 4.5 (b) can be rewritten by

$${}_kI = Y_s ({}_kV_1^r - {}_kV_1^i) \quad (\text{Eq 4.5.d})$$

Eq 4.5 (c) yields

$${}_kV_h^i = {}_kV_h^r - {}_kV_1^r + {}_kV_1^i \quad h=2,3,\cdots,H \quad (\text{Eq 4.5.e})$$

Combining Eq 4.5 (e) and (a) yields

$${}_kV = H {}_kV_1^i + (2 - H) {}_kV_1^r + 2 \sum_{h=2}^H {}_kV_h^r \quad (\text{Eq 4.5.f})$$

Eq 4.5 (f) and (d) involve only a single unknown voltage ${}_kV_1^i$. This unknown voltage can be obtained by solving the discretized current-voltage equation of the device. The other unknown voltages are then obtained by using Eq 4.5 (e). The unknown voltages for the first order device, which are a function of the reflected voltages, can be expressed as

$${}_k V_1^i = f[{}_k V_1^r, {}_{k-1} V_1^i, {}_{k-1} V_1^r, \sum_{h=2}^H {}_k V_h^r, \sum_{h=2}^H {}_{k-1} V_h^r]$$

$${}_k V_h^i = {}_k V_h^r - {}_{k-1} V_1^r + {}_{k-1} V_1^i \quad (\text{Eq 4.6})$$

It is obvious from Eq 4.6 that the unknown voltages are obtained by solving a single nonlinear equation at each time step.

1) Two-port devices

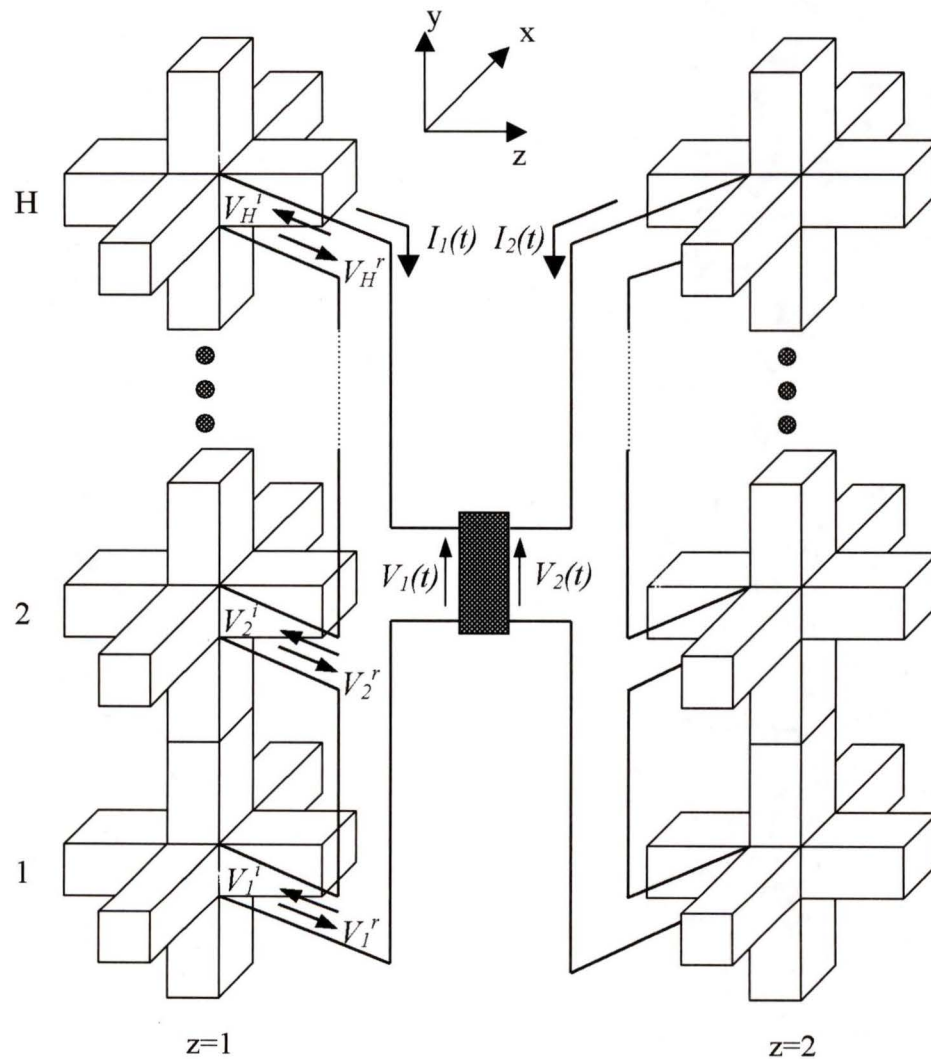


Figure 4.9 A schematic connection of a two-port device in the z-direction by two sets of stacked stubs

Two-port nonlinear active and passive devices can be modeled by means of two sets of stacked stubs (Figure 4.9). In this structure, the lumped device is connected between two adjacent stacked stubs in the z-direction and occupies H nodes in the y-direction. The z-directed link lines of the nodes equipped with a device stub must be terminated by an open circuit.

2) Embedding a lumped element in an inhomogeneous medium

Traditionally, stubs are added to the standard SCN mesh to modify the medium properties and the cell geometry. We also use stubs to connect lumped equivalent circuits. In the case described above, the device is embedded in a homogeneous medium with permittivity constant $\epsilon_r=1$. However, in order to embed the device in an inhomogeneous medium, additional stubs (port numbers 13~18) are employed to represent the characteristics of the computational region and other stubs (port numbers 19~21) are used to connect the device to the nodes. Usually, since only one of the three field components will be affected by the presence of the device, only one of three stubs is needed to connect the device. Since the others are not used, their admittances must be zero. A full 21×21 scattering matrix [31] for this purpose can be obtained by using Kirchhoff's laws and energy conservation.

4.3 Boundary Implementation

4.3.1 Modeling of one-port devices with Boundary Implementation in 2D-TLM

The boundary embedding technique (Figure 4.1 (b),(d)) provides a scheme for connecting the device without using stubs. In Figure 4.10, the link lines interfaced with the device volume are terminated by the lumped device circuit. Therefore, no

electromagnetic fields exist in the device volume. This causes some differences in results obtained using boundary and stub embedding techniques.

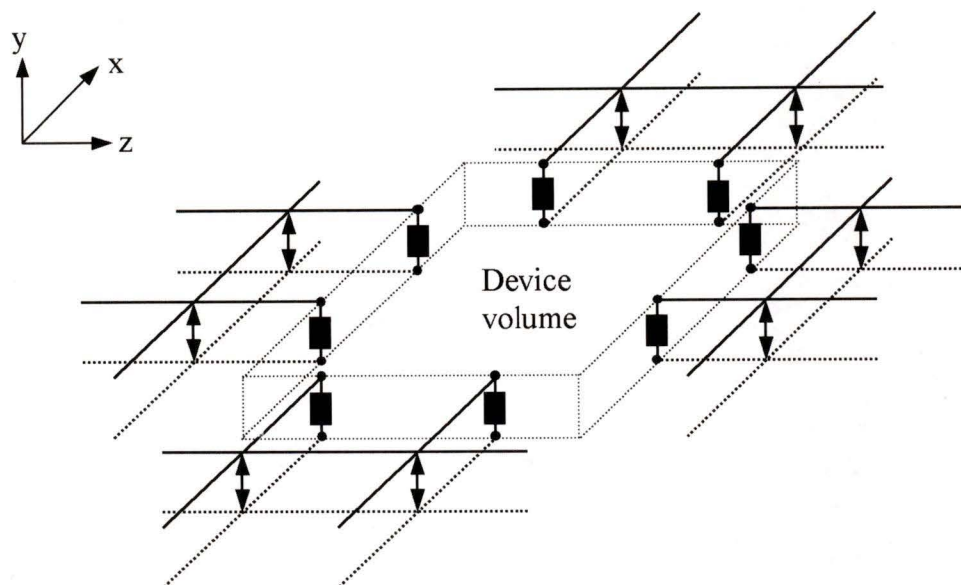


Figure 4.10 The layout of sub-devices in boundary implementation using 2D-TLM shunt node

Obviously, the layout in Figure 4.10 which shows independent sub-devices can only be used when the device is linear. If the device is non-linear, the properties of the sub-devices must be kept the same and depend on the total current and a space average of all voltages across the sub-devices at each time step.

4.3.2 Modeling of two-port devices with Boundary Implementation in 3D-TLM

Figure 4.11 shows the schematic connection of a two-port device by two sets of stacked link lines. Compared with Figure 4.9, this connection scheme has the advantage that it does not require the extended scattering matrix to include the device stub. This results in less computational demand. In node implementation, the connection between the device stub and the TLM node introduces an error that has the same effect as a discontinuity in the medium filling the propagation space. The scattering matrix for the

nodes equipped with the device stub is different from that for the nodes without the device stub, and must therefore be corrected. However, the boundary scheme does not introduce this kind of error.

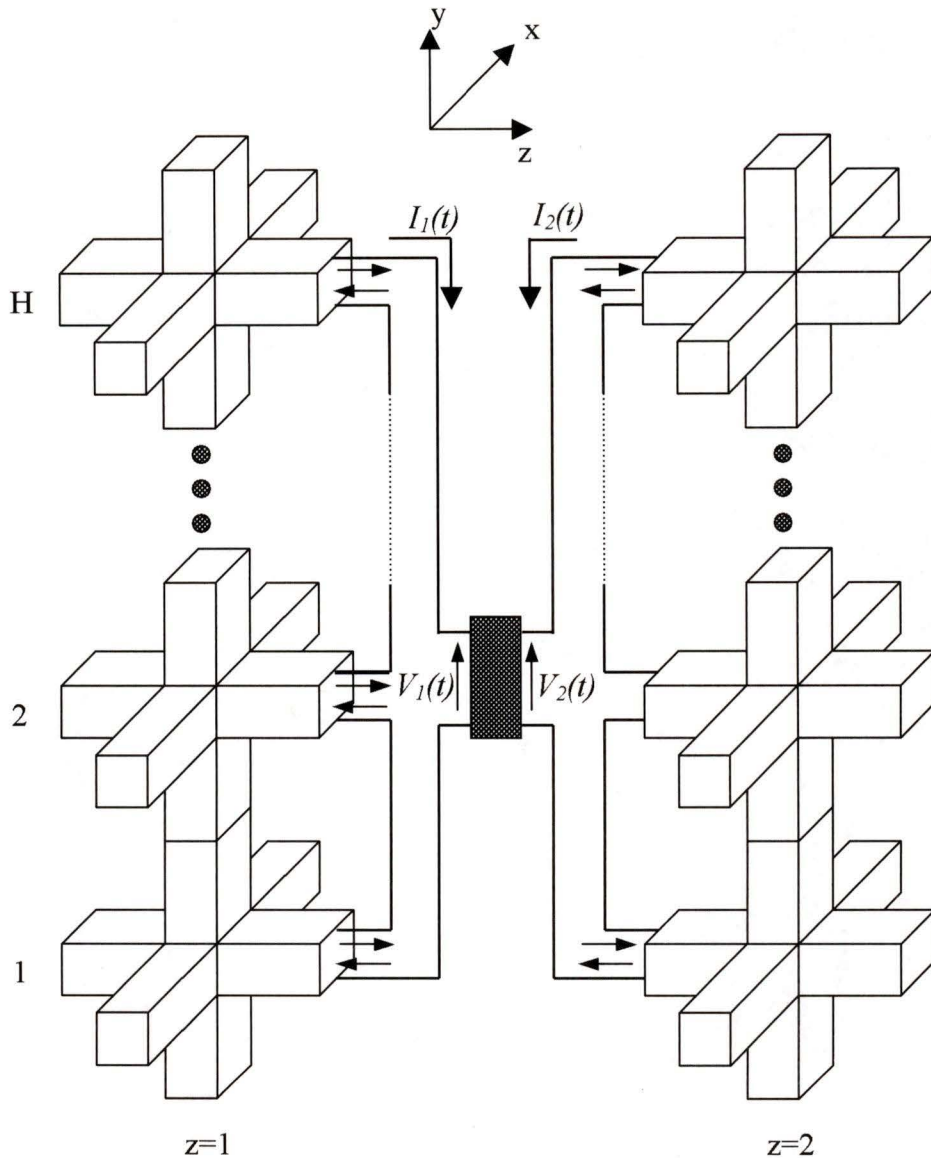


Figure 4.11 A schematic connection of a two-port device in the z -direction by two sets of stacked link lines

Another difference between boundary and node implementation is that no extra reference admittance for the transmission line connecting the device needs to be defined,

since it is simple. In 3D TLM, the characteristic admittance of the link lines is $1/\eta_0$ where η_0 is the characteristic impedance of free space. However, the characteristic admittance of the device stub is arbitrary. Usually, this value is chosen so that the reflection coefficient seen by the device into the node is null.

The unknown voltages incident from the device upon the node can be calculated using Equation 4.5 (a)~(f). Note that Equation 4.5 (a)~(f) is still valid except that the characteristic admittance of the device stub (Y_s) must now be replaced by the characteristic admittance of the link lines (Y_l).

4.4 Star-Type Implementation

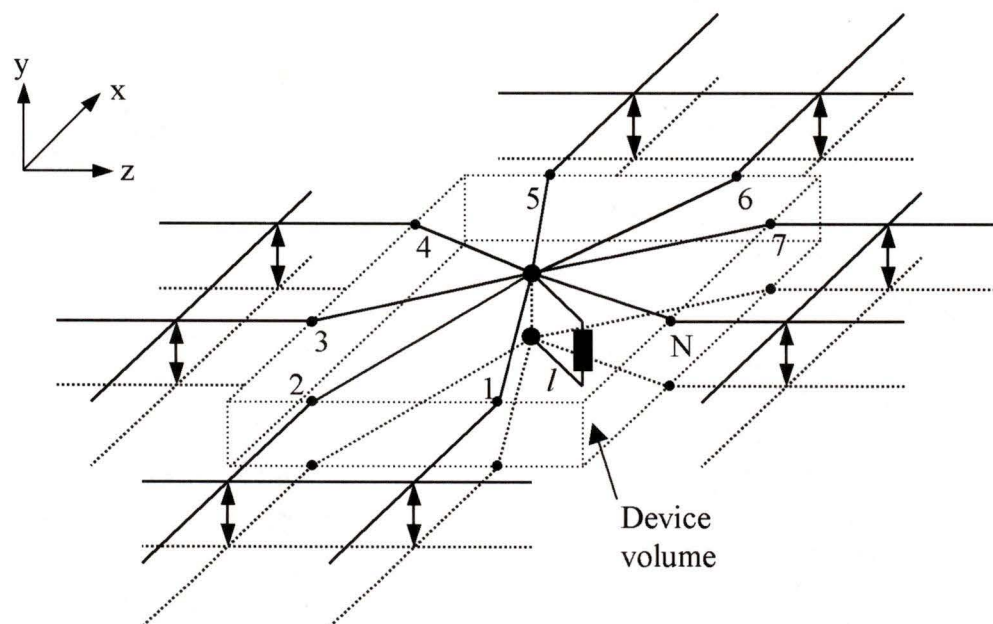


Figure 4.12 A schematic layout of star-type implementation in 2D-TLM shunt node

Figure 4.1. (e) and Figure 4.12 show the star-type device implementation. Here, the device is represented by a single lumped element that is connected centrally to N TLM transmission lines entering the boundary of the device volume by solving the

nonlinear device equation only once at each time step. The length of the transmission line connecting the device to N TLM transmission lines is zero.

The scattering matrix for this device-embedding scheme is given by

$$\begin{bmatrix} {}_k V_s^r \\ {}_k V_1^r \\ {}_k V_2^r \\ {}_k V_3^r \\ \vdots \\ {}_k V_n^r \end{bmatrix} = \begin{bmatrix} 0 & 1/n & 1/n & 1/n & \cdots & 1/n \\ 1 & (1-n)/n & 1/n & 1/n & \cdots & 1/n \\ 1 & 1/n & (1-n)/n & 1/n & \cdots & 1/n \\ 1 & 1/n & 1/n & (1-n)/n & \cdots & 1/n \\ \vdots & \vdots & \vdots & \vdots & \cdots & \vdots \\ 1 & 1/n & 1/n & 1/n & \cdots & (1-n)/n \end{bmatrix} \cdot \begin{bmatrix} {}_k V_s^i \\ {}_k V_1^i \\ {}_k V_2^i \\ {}_k V_3^i \\ \vdots \\ {}_k V_n^i \end{bmatrix} \quad (\text{Eq 4.7})$$

where ${}_k V_s^r$ represent the voltage impulses reflected on the star lines by the device at time step k , and ${}_k V_n^i$ are the incident voltage impulses on the n star lines. The voltage incident on the device is given by

$${}_k V_s^r = \frac{{}_k V_1^i + {}_k V_2^i + {}_k V_3^i + \cdots + {}_k V_n^i}{N} \quad (\text{Eq 4.8})$$

Note that the reference admittance for the device is chosen as N times the characteristic admittance of the star link lines. This condition decouples the incident and reflected voltage pulses of the device.

This technique is valid when the wavelength of interest is much larger than the size of the device volume. The extension of this approach to 3D problems is straightforward and therefore, is not discussed here.

4.5 Conclusion

In this Chapter, three kinds of device embedding techniques have been discussed. Node implementation is used to model the linear/nonlinear and one-/two-port devices by

means of stubs of length zero or $\Delta l/2$. The stubs, traditionally used to model the properties of the medium and cell geometry, have been employed to connect the equivalent device circuit to the node. A method used to embed the device in an inhomogeneous medium has also been presented.

It is shown that boundary implementation and star-type implementation are also suitable for embedding linear and nonlinear devices. In particular, the boundary scheme is less computational demanding and much simpler to implement.

On the other hand, boundary implementation removes field space from the inside of the device volume with the effect shown in Figure 4.3. However, it is possible to account for this effect by artificially adding appropriate energy storage to the equivalent circuit of the device in the form of reactances.

When selecting a particular type of implementation, the primary concern should be the need for modeling the physical configuration of a device as closely as possible. In this way we can ensure that the parasitic elements due to the geometry and topology of a particular device are properly accounted for. Accuracy has been verified by studying the convergence of the solution for a given geometry when the mesh size Δl is progressively reduced towards the infinitesimal limit. Extrapolation of results obtained with different mesh sizes using Richardson's approach is very reliable in the case of TLM field models, even in the presence of field singularities at sharp edges and corners.

Chapter 5

Comparison of Device Embedding Techniques

5.1 Introduction

In the previous chapter, we discussed the properties of three kinds of device embedding techniques and their schematic layouts in a TLM network. The embedding of one- and two-port devices in 2D- and 3D-TLM was also examined.

In the following, we compare the results obtained using these schemes for linear and nonlinear devices. We first derive the numerical expression representing the behavior of the specific device to be embedded and discretized them. In other words, the general expressions Eq 4.4 and 4.6 must be rewritten to obtain the unknown voltages incident from the device upon the TLM nodes. The numerical results obtained with each technique must then be analyzed and compared with the theoretical results. To minimize parasitic effects due to the finite volume of the devices and to test only the device equations and their connection to the TLM algorithm, we have performed simulations

involving 1D field distributions (Figure 5.1). This allows us to compare the numerical results directly with circuit-based results obtained both analytically and with SPICE.

Note that the embedding techniques described in chapter 4 and their validation procedure are the basis for a connection between SPICE and the TLM algorithm that will be discussed in the next chapter. In this chapter, we test all three embedding techniques for several linear and nonlinear devices. For the node implementation we have only considered device stubs of zero length.

The modeling of linear first-order devices is discussed first. The embedding of nonlinear passive and active devices is then described.

5.2 Modeling of Linear First-Order Devices

5.2.1 Derivation of the formulation for the linear devices

In this section, the first order differential equations of a linear device such as a capacitor or an inductor will be reviewed and discretized using a central difference scheme (Eq 4.3) to obtain the unknown voltage incident from the device upon the TLM nodes.

The current-voltage equation of a capacitor is

$$i(t) = C \frac{dV(t)}{dt} \quad (\text{Eq 5.1})$$

Discretizing Eq 5.1 with a central difference scheme (Eq 4.3) yields

$$\frac{{}_k I + {}_{k-1} I}{2} = \frac{C}{\Delta t} ({}_k V - {}_{k-1} V) \quad (\text{Eq 5.2})$$

Substituting Eq 4.5 (d) and (f) into Eq 5.2 gives

$${}_k V_1^i = \frac{\left(\frac{1}{2} Y_s + \frac{(H-2)C}{\Delta t}\right) {}_k V_1^r - \frac{2C}{\Delta t} \sum_{h=2}^H {}_k V_h^r + 0.5 {}_{k-1} I + \left(\frac{C}{\Delta t}\right) {}_{k-1} V}{\frac{1}{2} Y_s + \frac{HC}{\Delta t}} \quad (\text{Eq 5.3})$$

and other new incident voltages (${}_k V_2^i \dots {}_k V_h^i$) are obtained by Eq 4.5 (e). Note that the value of the capacitance is divided by the number of sub-devices connected in parallel. Similar relations can be written for an inductor.

5.2.2 Simple low- and high-pass filter implemented by Node implementation

A simple low-pass filter represented by a capacitor and a high-pass filter represented by an inductor are simulated in 3D-TLM.

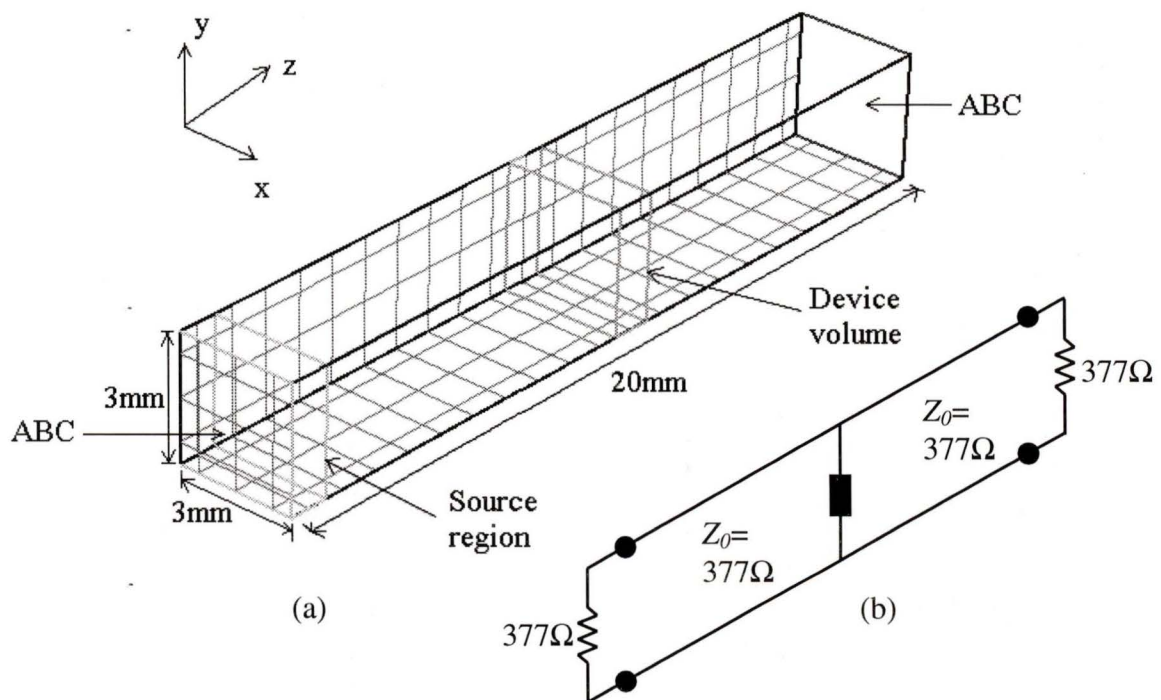


Figure 5.1 The geometry of a parallel-plate waveguide containing device volume (a) and its 1D equivalent circuit (b)

The devices are connected to the TLM network by a set of stacked stubs (Figure 4.7). Figure 5.1 (a) shows the geometry of a parallel-plate waveguide into which those filters are embedded as devices distributed in the device volume. Its 1D equivalent lumped circuit with the characteristic impedance $Z_0=377\Omega$ is shown in Figure 5.1 (b). This structure is discretized into $3\Delta x \times 3\Delta y \times 20\Delta z$ where $\Delta x = \Delta y = \Delta z = \Delta l = 1mm$. The computation region is filled with air. Hence, the characteristic impedance of the parallel-plate waveguide is 377Ω . Three sub-capacitors are distributed along the x-direction. This 3D-TLM structure is equivalent to a perfect one-dimensional problem so that its characteristics can be predicted theoretically.

The S-parameters of those filters are drawn in Figure 5.2. Excellent agreement between theoretical and numerical results from TLM and FDTD is obtained. The 2D-FDTD [16] simulation has been performed using Mur's first-order absorbing boundary conditions [32].

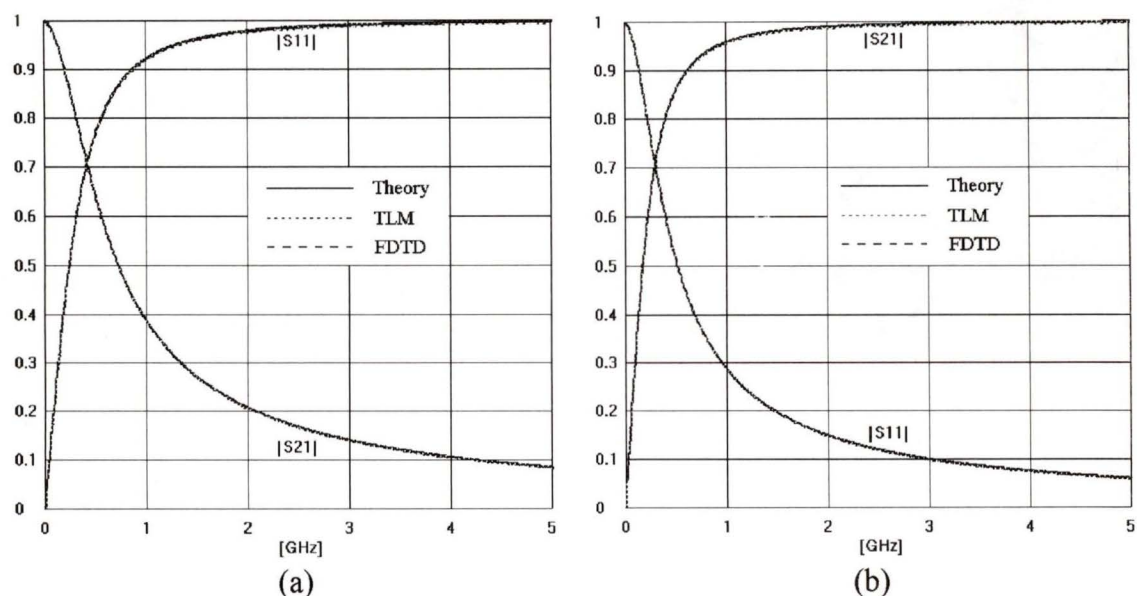


Figure 5.2 S-parameters of low-pass filter (a) and high-pass filter (b)

The values of capacitance and inductance are 2pF and 0.1μH, respectively. Here, the device stubs of length zero are used. Therefore, the extra reactance introduced by the stubs of length $\Delta/2$ which may cause a discrepancy between simulated and theoretical results has been eliminated. This extra reactance can be evaluated as follows:

The input admittance (Y_{in}) of an open stub of length $\Delta/2$ for low frequencies is given by

$$Y_{in} = jY_s \tan\left(\frac{\omega\Delta}{2v_{TL}}\right) \approx jY_s \frac{\omega\Delta}{2v_{TL}} = j\omega C_s \quad (\text{Eq 5.4})$$

From Eq 5.4, the parasitic capacitance of a stub C_s is

$$C_s = \frac{Y_s \Delta}{2v_{TL}} \quad (\text{Eq 5.5})$$

where Y_s denotes the characteristic admittance of the device stub, v_{TL} represents the velocity of propagation in the stub, and Δ is the spatial mesh size.

The parasitic inductance of the stub L_s is of the order of $(\Delta l)^2$. This value is small enough to be negligible. However, the total extra capacitance introduced by the device stubs of length $\Delta/2$ in device volume in Figure 5.1 is given by

$$C_{st} = \frac{W}{H} C_s = \frac{4}{Z_{TL}} \Delta l = \epsilon_0 \Delta l = 8.854 \text{ fF} \quad (\text{Eq 5.6})$$

and cannot be neglected. In fact, its presence gives rise to a parasitic resonance with the inductance that occurs at

$$f_0 = \frac{1}{2\pi\sqrt{LC_{st}}} = 5.35 \text{ GHz} \quad (\text{Eq 5.7})$$

The resonance causes undesired numerical error. However, it can be seen from 5.2 (b) and Eq 5.7 that no extra reactance exists and infinite resonance frequency is brought about when the length of the device stub is zero. Such undesired parasitic reactance can also be eliminated by using the star-type and the boundary implementations.

5.2.3 The modeling of a narrow band-stop filter by a star-type implementation

As mentioned in section 4.4, star-type implementation enables us to represent the behavior of the device by a single lumped element. As a result, the computational effort can be reduced and the effect of parasitic reactance can be avoided. This scheme is demonstrated using the same TEM transmission line as in Figure 5.1.

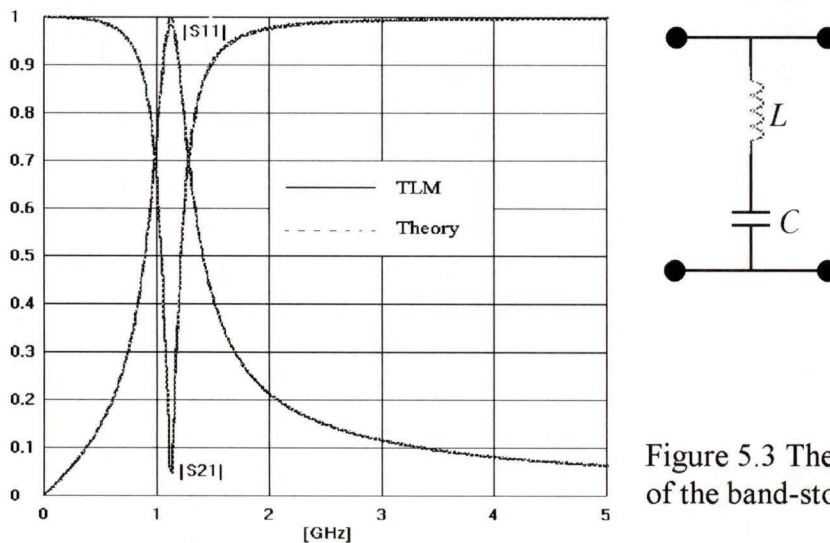


Figure 5.3 The S-parameters of the band-stop filter

Figure 5.3 shows the S-parameters of the series resonance circuit composed of an inductor of inductance $0.1\mu\text{H}$ and a capacitor of capacitance 0.2pF in a 2D-TLM network. It can be seen from Figure 5.3 that there is no parasitic resonance effect introduced by the device stubs of length $\Delta l/2$.

5.3 Modeling of Nonlinear Passive and Active Devices

5.3.1 Push-Pull Transmission-Line Oscillator

We also consider a push-pull oscillator comprising two identical Tunnel diodes. Figure 5.4 shows the oscillator featuring a slightly off-centered biasing arrangement. The I-V characteristic of the diode (Eq 3.5) is plotted in Figure 3.1.

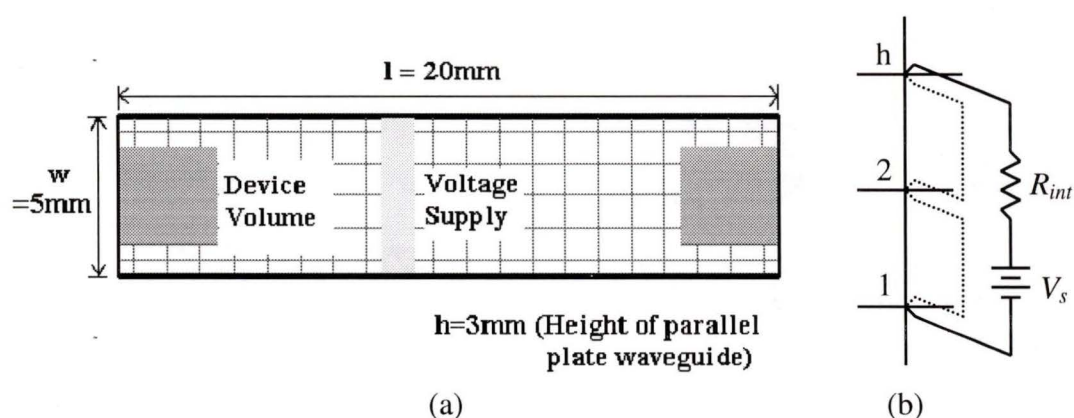


Figure 5.4 (a) The transmission line oscillator (b) stacked biasing circuit of height h

The nonlinear current-voltage characteristic of the diode is specified in Table 1.

Peak Current	Peak Voltage	Valley Current	Valley Voltage	Forward Peak Voltage
(I_p)	(V_p)	(I_v)	(V_v)	(V_{fp})
1mA	65mV	0.14mA	350mV	510mV

Table 1. Specifications of the Tunnel diodes used in the oscillator in Figure 5.4

In addition the diode has a series resistance of $R_s=4\Omega$ and a shunt capacitance of $C_p=5\text{pF}$ (Figure 5.5).

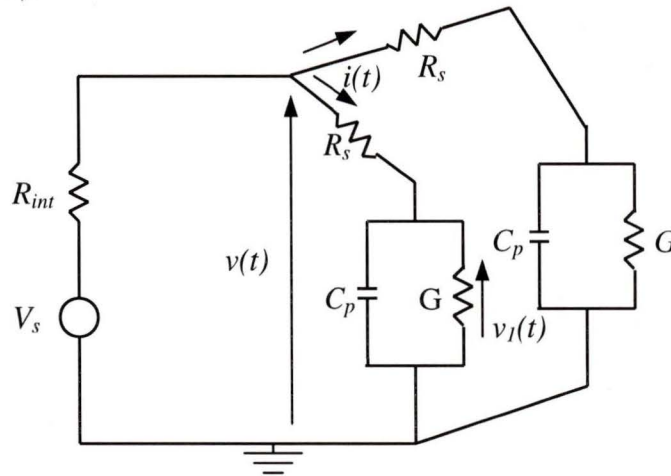


Figure 5.5 Equivalent DC circuit of the push-pull transmission-line oscillator. This circuit is only valid at dc.

The diode has a biasing point $I_0=0.73872\text{mA}$ and $V_0=0.15\text{V}$. The DC bias source supplies 0.2V and is positioned slightly off-centered to start the oscillations. Once the value of the DC bias source is determined, the source internal resistance R_{int} must be calculated so that the diode operates at the desired operating point (Figure 5.6).

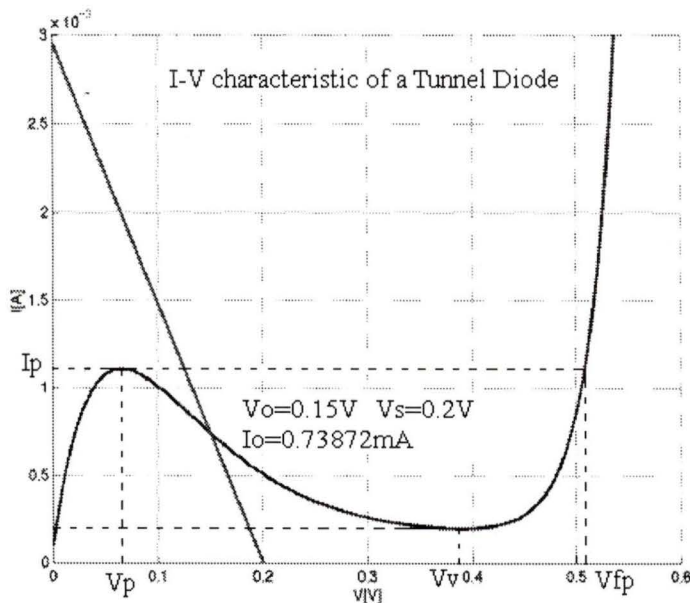


Figure 5.6 I-V characteristic of a tunnel diode and its biasing point

The source resistance is given by

$$R_{\text{int}} = \frac{1}{2} \left(\frac{V_s - V_o}{I_o} - R_s \right) \quad (\text{Eq 5.8})$$

and the maximum current at $V_1=0$ is

$$i_{\text{max}} = \frac{V_s}{2R_{\text{int}} + R_s} \quad (\text{Eq 5.9})$$

The unknown voltages incident from the device upon the nodes can be calculated as described in section 4.2.2 and given by

$${}_k V_1^i = \frac{1}{H + WR_{\text{int}} Y_s} \left[(H - 2 + WR_{\text{int}} Y_s) {}_k V_1^r - 2 \sum_{h=2}^H {}_k V_h^r + {}_k V_s \right]$$

$${}_k V_h^i = {}_k V_h^r - {}_k V_1^r + {}_k V_1^i \quad h = 2, 3, \dots, H \quad (\text{Eq 5.10})$$

The equation of the equivalent tunnel diode is given by

$$i(t) = C \frac{dv_1(t)}{dt} + i_1(v_1(t)) \quad (\text{Eq 5.11})$$

where $v_1(t) = v(t) - R_s i(t)$ and $i_1(t)$ is the current flowing in the conductance. The discrete form of Eq 5.11 obtained by central differencing is then given by

$${}_k I_{+k-1} - I = \frac{2C}{\Delta t} ({}_k V_1 - {}_{k-1} V_1) + {}_k I_1({}_k V_1) + {}_{k-1} I_1({}_{k-1} V_1) \quad (\text{Eq 5.12})$$

In order to obtain the new voltages incident from the device upon the nodes, Eq 5.12 is solved numerically at each time step by Newton's method [33].

Figure 5.7 shows the transient behavior of the push-pull oscillator in which the diodes were embedded in a 3D TLM network using a $3\Delta l \times 3\Delta l \times 3\Delta l$ and a $1\Delta l \times 1\Delta l \times 1\Delta l$ implementation, respectively.

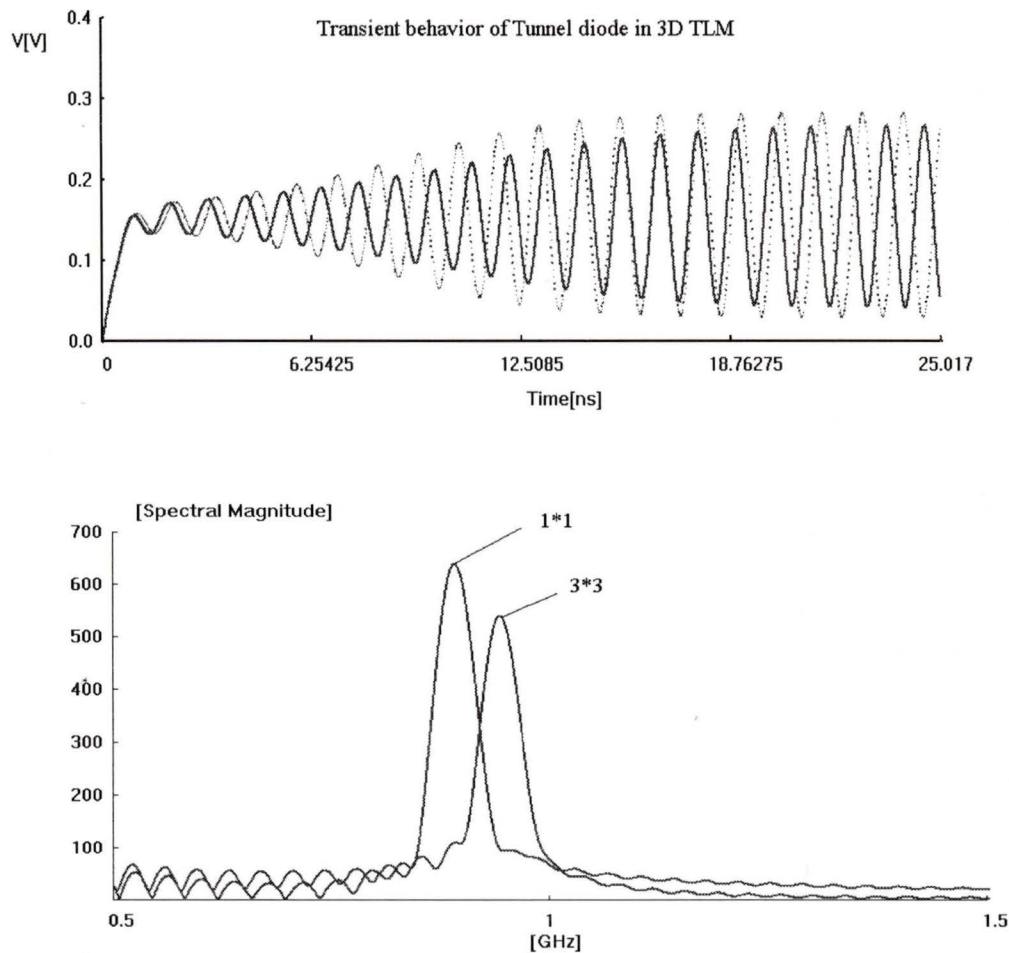


Figure 5.7 Transient behavior and frequency response of the push-pull oscillator by 3D-TLM network (dotted line : $1*1$, solid line : $3*3$).

There is an obvious difference in the magnitude and phase of the two oscillators due to the differences in device volume and to the interaction between the separated sub-devices.

Figure 5.8 depicts the time domain responses of the tunnel diode oscillator when the diodes are occupying the same volume, but are implemented using node and boundary implementations. In the node implementations case, nine sub-devices are distributed over a $3\Delta \times 3\Delta \times 3\Delta$ volume. In the boundary implementation case, nine instead of 12 sub-devices are placed on the lateral surface of the diode volume.

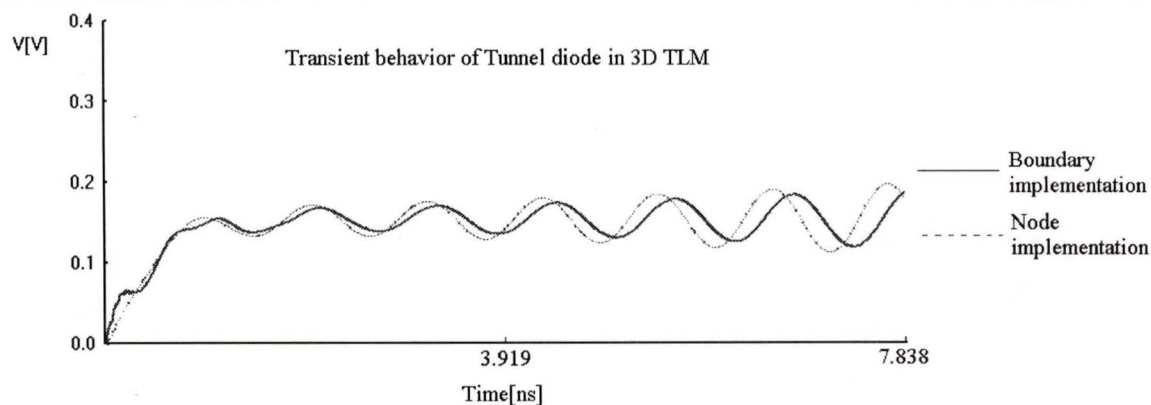


Figure 5.8 Time domain responses of a tunnel diode obtained with the node and boundary device embedding techniques.

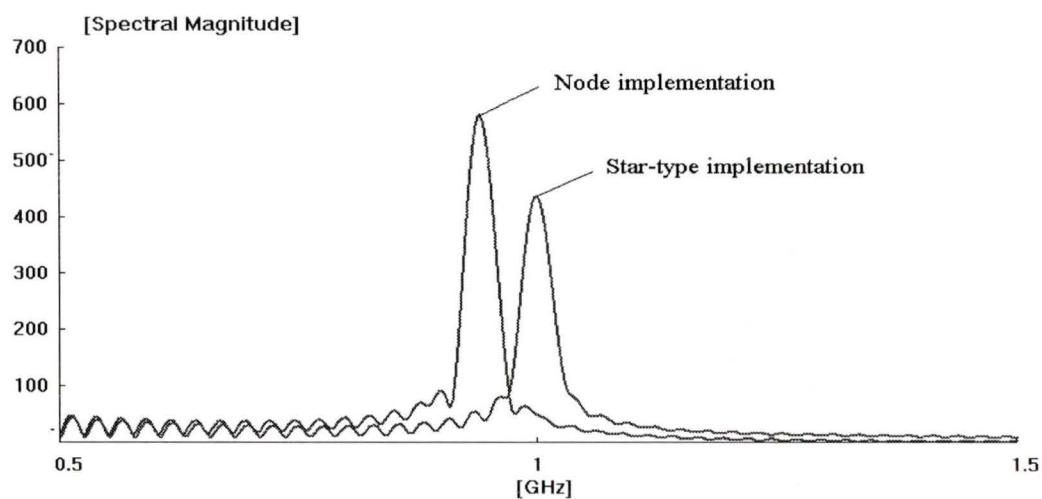
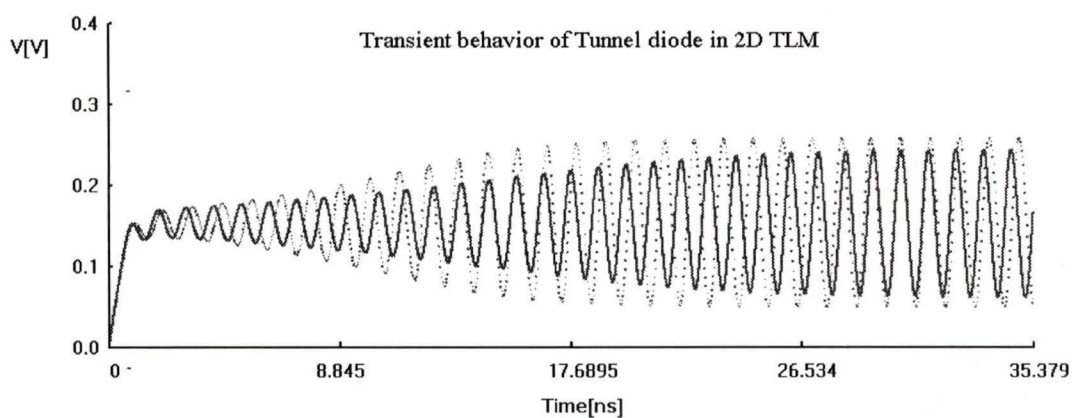


Figure 5.9 Comparison of the transient behavior and frequency response of the push-pull diode simulated by the node (dotted line) and star-type device embedding technique (solid line) in 2D-TLM.

Figure 5.9 shows the transient behavior and frequency response of the push-pull oscillator simulated by node implementation (dotted line) and star-line implementation (solid line) in 2D-TLM. The phase difference between these two implementations is a direct consequence of the differences in energy stored inside the device volume.

5.3.2 P-N Junction Diode

The simplest nonlinear device, a p - n junction diode, is modeled to compare the three embedding techniques. The nonlinear behavior of the diode is described by the formulae (Eq 3.2, 3.3 and 3.4). A similar approach used in section 5.3.1 to obtain the new voltages incident from the device upon the nodes can be applied. The current-voltage equation of the equivalent p - n junction diode is given by

$$i(t) = I_s \left[e^{\frac{qv(t)}{kT}} - 1 \right] + [C_j(v(t)) + C_d(v(t))] \frac{dv(t)}{dt} \quad (\text{Eq 5.13})$$

and its discrete form is given by

$${}_k I + {}_{k-1} I = I_s \left[e^{\frac{q_k V}{kT}} - 1 \right] + I_s \left[e^{\frac{q_{k-1} V}{kT}} - 1 \right] + [C_j({}_k V) + C_d({}_k V) + C_j({}_{k-1} V) + C_d({}_{k-1} V)] \frac{{}_k V - {}_{k-1} V}{\Delta t} \quad (\text{Eq 5.14})$$

This discretized equation is obtained by averaging the capacitance at the time steps $k\Delta t$ and $(k-1)\Delta t$. Figure 5.10 shows the frequency response of a p - n junction diode embedded in a 2D-TLM network by the node and the star line embedding techniques.

[Spectral Magnitude]

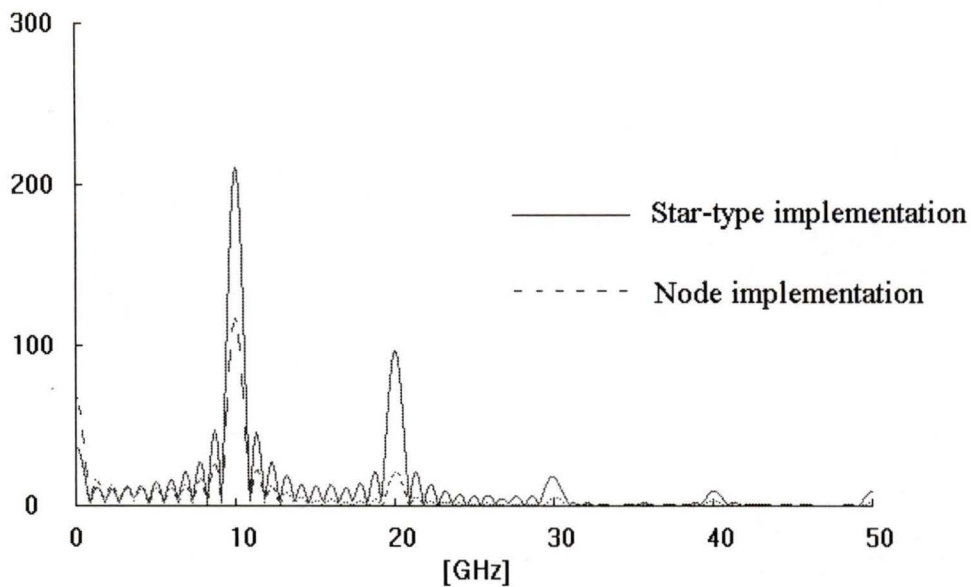


Figure 5.10 Frequency response of a p-n junction diode obtained by the star-type device embedding technique in 2D-TLM

The diode is placed at one extremity of a TEM transmission line discretized with five TLM cells in transverse direction, while a sinusoidal source is used to excite the line at the other end. The graph clearly shows a DC component and the higher order harmonics at 20, 30, and 40 GHz.

The values for the excitation and diode parameters are

Sinusoidal excitation:	10 GHz
Zero-bias junction capacitance:	0.1 pF
Transit time:	0.1 ns
Saturation current:	10^{-14} A
Built-in voltage:	0.8 V

5.3.3 The Bipolar Junction Transistor

The node implementation to embed two-port nonlinear devices is described in section 4.2.2. In the following, the equivalent circuit of a bipolar junction transistor in

Figure 3.2 is modeled. The two nonlinear-coupled equations (Eq 3.6) representing the behavior of a bipolar junction *npn* transistor can be derived [28] and solved numerically to obtain the new voltage incident from the device upon the nodes.

However, the numerical computation of two nonlinear coupled equations is very difficult. Thus, the optimization toolbox in Matlab version 5.3.0 was used for solving them. This procedure is very time-consuming and requires extra care in programming them. Hence, in order to avoid the need for such difficult derivations of the discretized form of the equivalent circuit equations, we have investigated the possibility to connect SPICE to the TLM algorithms.

5.4 Conclusion

In this chapter, the properties of three different embedding techniques for several kinds of devices have been described. Simple linear devices were modeled first, and then several nonlinear passive and active devices were embedded in a TLM network.

Numerical results obtained with different embedding techniques were compared with theoretical results. Good agreement was achieved. Therefore, we can conclude that the three different embedding techniques are suitable for connecting a device to the TLM node even though they show slight differences in results due to their own embedding properties. This can easily be compensated by the addition of connective reactance. It has also been found that it is not straightforward to solve the discretized form of the extensive nonlinear equivalent circuit equations. The methodology to reduce such a heavy computational effort will be discussed in detail in the next chapter.

Chapter 6

The Connection between SPICE and TLM

6.1 Introduction

So far, we had to derive the formulae describing the behavior of devices in order to obtain the unknown voltages incident from the devices upon the TLM nodes. This approach is time consuming and requires extra programming effort to solve the nonlinear equations representing the characteristics of the devices. In the case of very stiff nonlinearities, the time step used in the field solution may be even too large to accurately integrate them, and instabilities may result. It is possible to avoid these problems by solving the device equations separately using SPICE. In this chapter, we will discuss the connection between SPICE and TLM and exploit its powerful features.

TLM has the advantage that electromagnetic fields can be represented by voltages and currents in a network of transmission lines. This enables us to couple SPICE [34], version 2G.6, directly and easily with TLM through a data pipe. SPICE was developed

for analyzing IC designs. It is still widely used in industry and universities. We can thus take full advantage of all existing device models in SPICE and do not need to formulate them again. All other features supported by SPICE like temperature sensitivity are available at no extra cost.

6.2 Connection between SPICE and TLM

As shown in Chapter 4, the voltage ${}_kV^i$ incident from the device upon the node (Figure 4.5) is a function of the voltage ${}_kV^r$ reflected from the node into the device and the incident and reflected voltages at the previous time step for a first-order device. We should set up the proper SPICE model to obtain the unknown new incident voltage ${}_kV^i$. This approach is described below.

Figure 6.1 shows a circuit layout in SPICE obtained with Thevenin equivalent circuits of the device stub for calculating the incident voltage (${}_kV^i$) of one-port (a) and two-port (b) devices. The value of the DC source in the SPICE model is thus $2{}_kV^r$ and the value of the resistor (Z_s) is the characteristic impedance of the device stub.

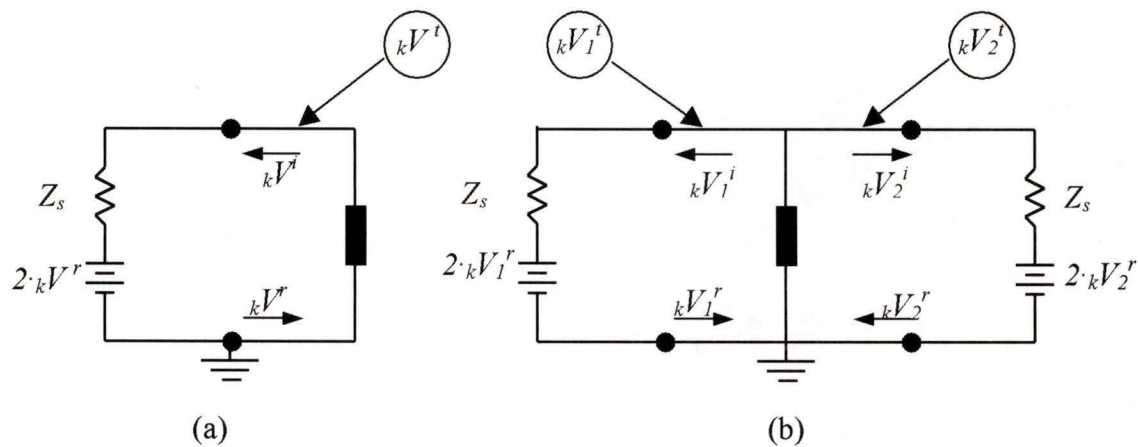


Figure 6.1 The schematic in SPICE for one-port (a) and two-port (b) devices

In SPICE, it is impossible to distinguish between the incident and reflected voltages. Only the total voltage can be measured. Therefore, the incident voltage ${}_kV^i$ can be obtained by

$${}_kV^i = {}_kV^t - {}_kV^r \quad (\text{Eq 6.1})$$

Note that the Thevenin equivalent circuit is valid only for one TLM time-step. This means the parameter values in the SPICE model will be changed at next time-step. These values can be changed through the data pipe. This applies to both one- and two-port devices. The procedure described above is summarized in the flow chart in Figure 6.2

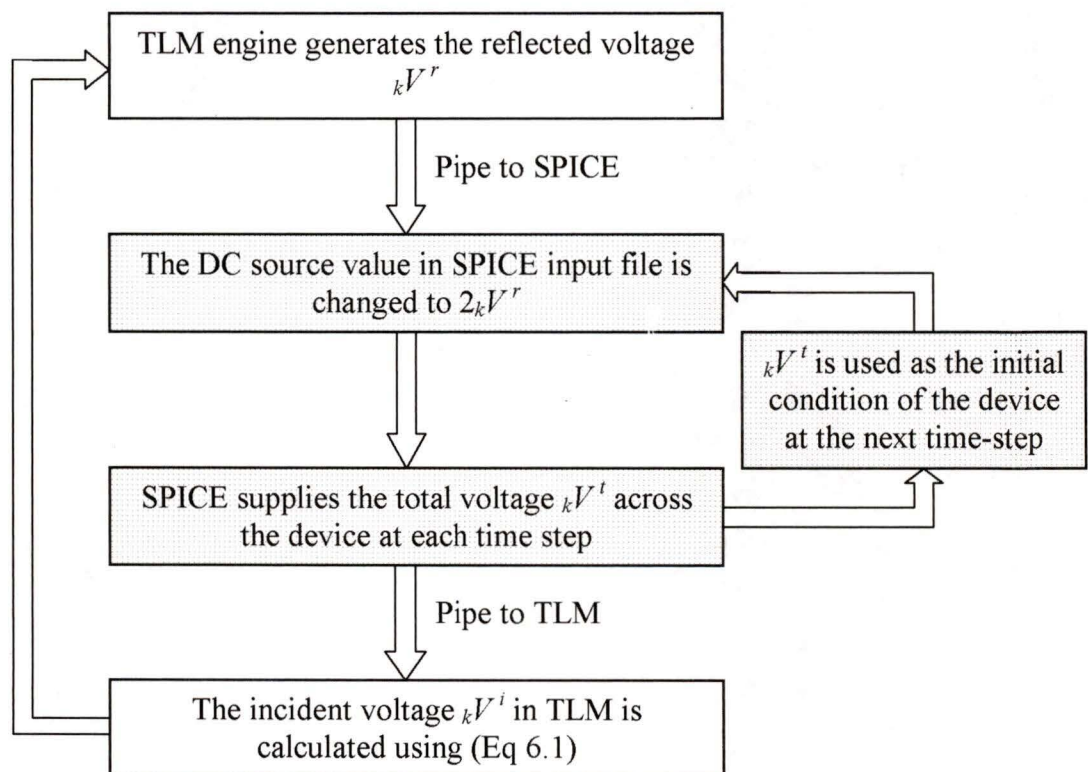


Figure 6.2 The flow chart representing the coupling between SPICE and TLM

Note that SPICE [28][35] performs a transient analysis using the initial condition (voltage or current) of the devices. This enables us to assume that the value of the DC source is constant during each TLM time step.

6.3 Validation of the SPICE-TLM Algorithm

In this section, the SPICE-TLM algorithm is verified for both lumped element passive and nonlinear active devices. Figure 6.3 shows the S-parameters of the high-pass filter simulated using the geometry shown in Figure 5.1. Here, the value of the inductor is 0.1nH. SPICE has also been coupled with 2D-FDTD using Ampere's Law [36]. The computational region at the extremities of the structure has been truncated by Berenger's split-field PML [37]. Good agreement is obtained using both 2D SPICE-TLM and 2D SPICE-FDTD.

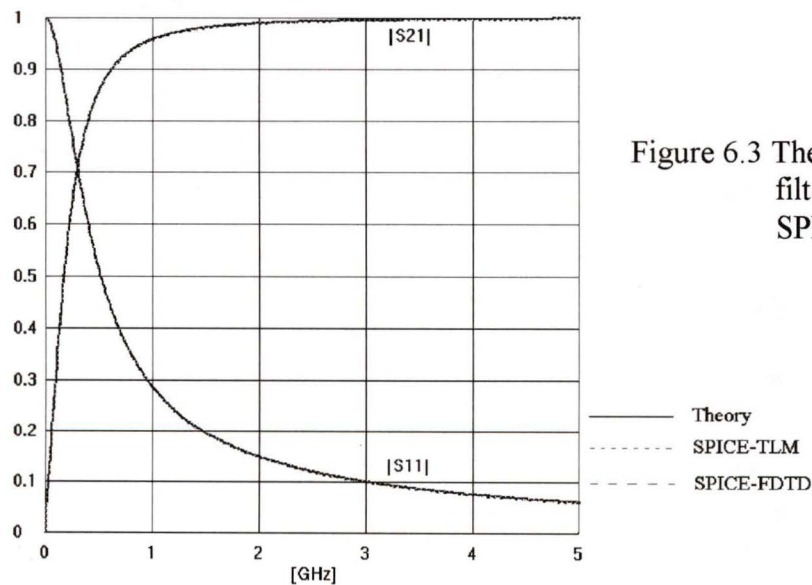


Figure 6.3 The S-parameters of the high-pass filter obtained by SPICE-TLM, SPICE-FDTD and Theory.

The band-pass filter has also been modeled with SPICE-TLM using the geometry shown in Figure 5.1. The values of the inductor and the capacitor are 1nH and 2pF, respectively. The S-parameters and their phases are shown in Figure 6.4. The device stub of length zero has been employed to minimize the extra reactance introduced by the device stub of length $\Delta/2$.

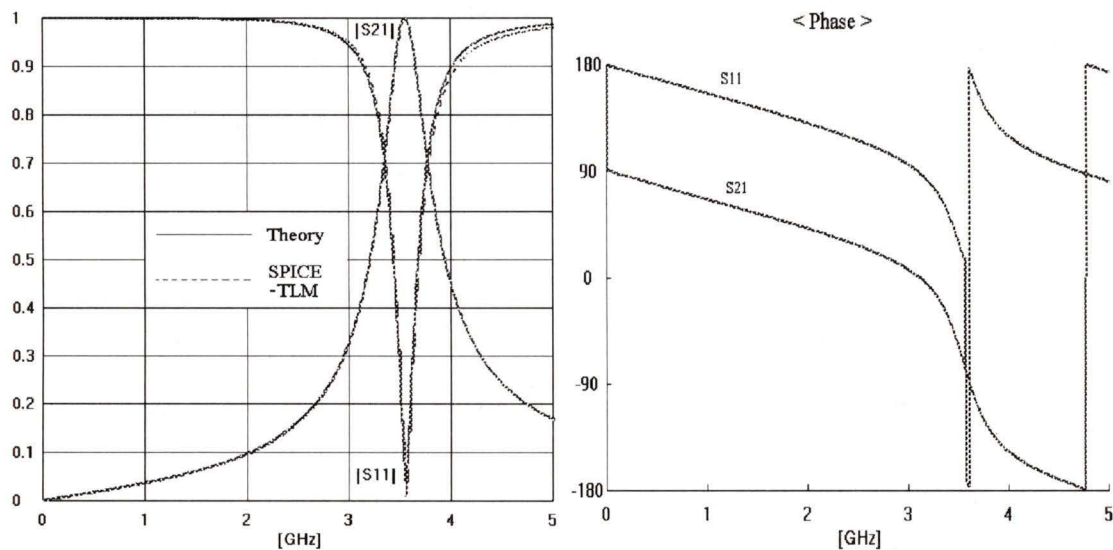


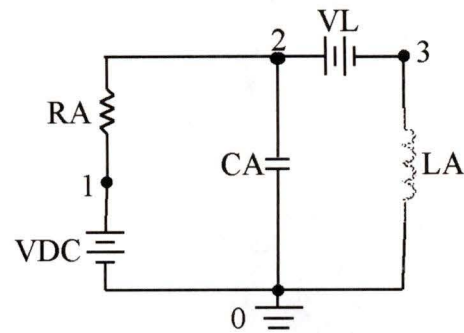
Figure 6.4 The S-parameters and their phases obtained by SPICE-TLM (solid line) and Theory (dotted line)

Note that in SPICE, version 2G.6, an inductor requires the value of the current as initial condition. The inductor current cannot be measured directly in SPICE. Only current flowing in independent sources can be measured. To circumvent this, we connect a 0 DC voltage source in series with the inductor. Circuits are defined in SPICE by means of an input file which lists each circuit element and indicates how each is connected using node numbers. Each circuit element in SPICE is connected to a node. SPICE then reads the input file and uses Kirchhoff's current law to create a system of equations for the circuit. The SPICE input file for a lumped element band-pass filter is presented below.

```

VDC 1 0 0
RA 1 2 399.6
CA 2 0 0.6667E-12 IC=0
VL 2 3 0
LA 3 0 0.3E-8 IC=0
.TRAN 0.235863P 2.35863P UIC
.PRINT TRAN V(2,0) I(VL)
.END

```



Here, the DC voltage source (VDC) is updated at each time step by the voltage reflected by a TLM node into the device. The values of the capacitor are divided by the number of the sub-devices connected in parallel, while the values of the inductor are multiplied by it. The quantity RA 399.6 indicates the characteristic impedance of the device stub. This value is given by

$$R = \frac{H}{Y_s} = 399.6\Omega \quad (\text{Eq 6.2})$$

where H is the height of the device and Y_s is the characteristic admittance of the device stub. 2.35863P is the time-step in TLM and SPICE runs during this time. 0.235863P is the fixed integration time-step in SPICE. It can be changed to integrate more accurately. The initial condition (IC, UIC) is used for the first DC transient analysis (.TRAN). The quantities V(2,0) and I(VL) are the measured voltage across, and current flowing through, the device. V(2,0) is sent to TLM through the data pipe to obtain the new voltage incident from the device upon the nodes, and I(VL) is used to update the initial conditions of the device for the next time-step.

In order to verify the SPICE-TLM algorithm for nonlinear active devices, a simple amplifier (Figure 6.5) was analyzed featuring an ideal BJT transistor inserted into a parallel-plate waveguide of size $3 \Delta x \times 3 \Delta y \times 20 \Delta z$ where $\Delta x = \Delta y = \Delta z = \Delta l = 1 \text{ mm}$. The lumped resistive input and output voltage sources as well as the BJT transistor are inserted by means of two sets of stacked stubs (Figure 4.9) or stacked link lines (Figure 4.11). The source delivers $V_s = 0.88 + 0.08 \cdot \sin(2\pi ft)$ where $f = 220 \text{ MHz}$, $R_{int} = 1200 \Omega$, $V_c = 5 \text{ V}$ and $R_c = 377 \Omega$.

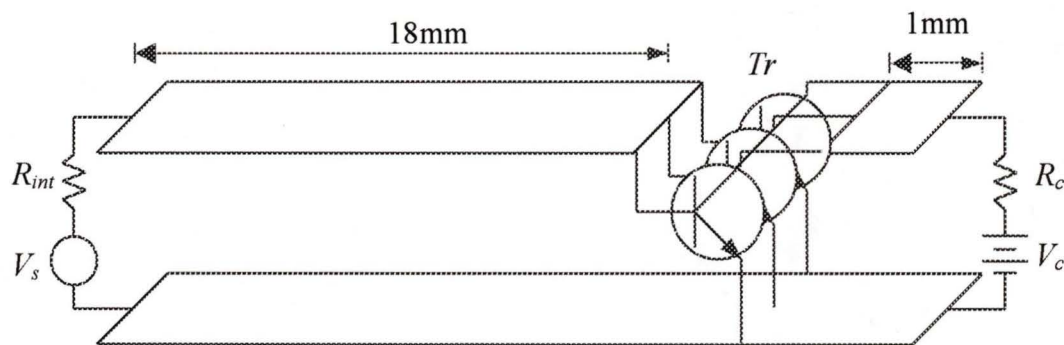


Figure 6.5 A simple amplifier with a BJT transistor.

Figure 6.6 and 6.7 show the base-emitter voltage and the collector-emitter voltage at the transistor obtained with a full SPICE simulation and with a coupled 3D SPICE-TLM algorithm using node and boundary implementations, respectively. Excellent agreement between the three results is obtained. The extra capacitance introduced by the device stubs and the finite distance between the source and the transistor have been taken into account when creating the equivalent SPICE circuit.

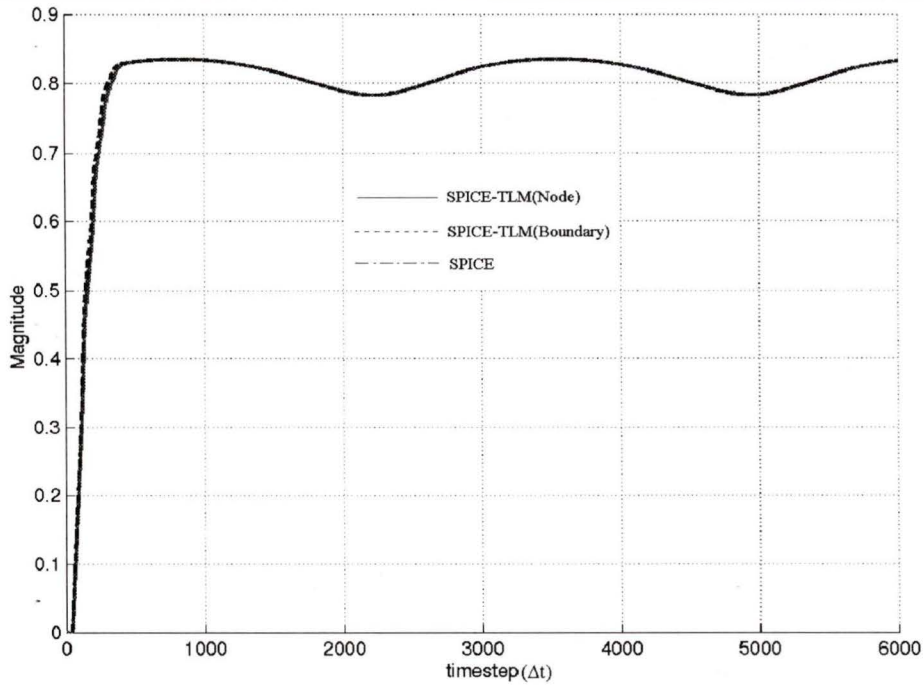


Figure. 6.6 The base-emitter voltage computed with SPICE alone (dash dotted line), SPICE-TLM using node implementation (solid line), and SPICE-TLM using boundary implementation (dotted line).

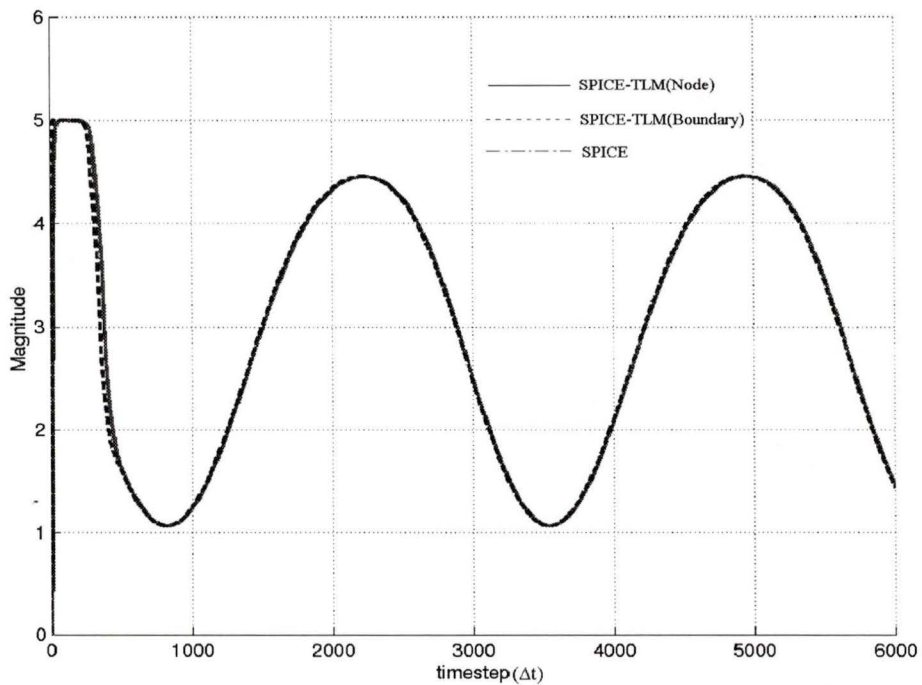
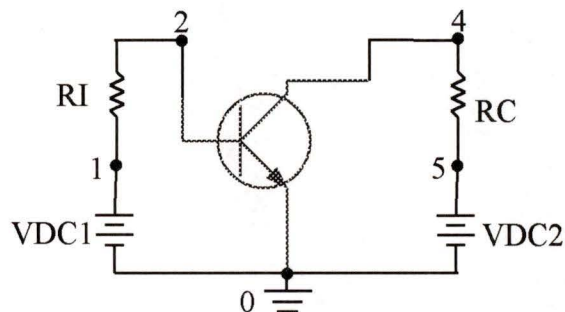


Figure. 6.7 The collector-emitter voltage computed with SPICE alone (dash dotted line), SPICE-TLM using node implementation (solid line), and SPICE-TLM using boundary implementation (dotted line).

The input file used for the transistor example is presented below. Note that in order to model a transistor with I_S (saturation current), this value must be divided by the number of sub-devices connected in parallel one another in SPICE input file.

```
VDC1 1 0 0
RI 1 2 282.56
% RI 1 2 1130.19 for boundary scheme
QTR 4 2 0 AMP IC=0,0
RC 4 5 282.56
% RC 4 5 1130.19 for boundary scheme
VDC2 5 0 0
.MODEL AMP NPN(IS=0.3333E-16)
.TRAN 0.16678P 1.6678P UIC
.PRINT TRAN V(2,0) V(4,0)
```



Here, QTR is the name of the transistor and AMP is the model name. $V(2,0)$ and $V(4,0)$ measure the base-emitter and the collector-emitter voltages, respectively. These quantities are used as initial conditions for the device and to obtain the new voltages incident from the device upon the TLM nodes. The impedance of the set of stacked stubs used in Figure 6.5 is 282.56Ω and the impedance of the set of stacked link lines is 1130.19Ω .

The charge-storage effects of the BJT transistor are represented by parameters such as C_{JE} , C_{JC} , TF , and TR . C_{JE} and C_{JC} indicate base-emitter zero-bias depletion capacitance and base-collector zero-bias depletion, respectively. TF is the ideal forward transit time and TR is the ideal reverse transit time. The BJT transistor with the charge-

storage effect is also inserted into the parallel-plate waveguide in Figure 6.5. The source delivers $V_s=0.875+0.075\cdot\sin(2\pi ft)$ where $f=2\text{GHz}$, $R_{int}=1000\Omega$, $V_c=5\text{V}$ and $R_c=377\Omega$.

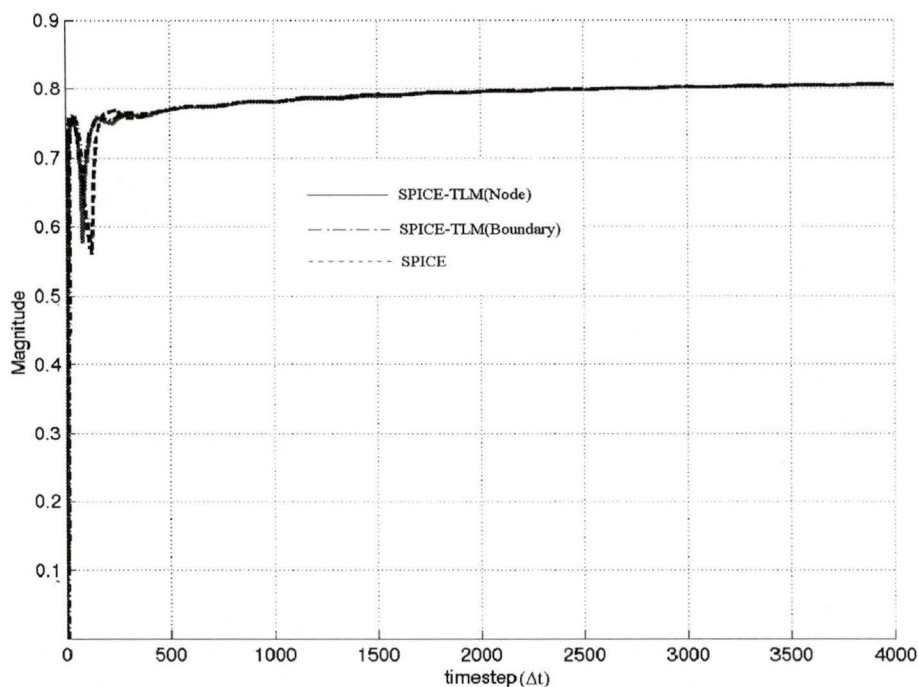


Figure 6.8 The base-emitter voltage computed with SPICE alone (dotted line), SPICE-TLM using node implementation (solid line), and SPICE-TLM using boundary implementation (dash dotted line).

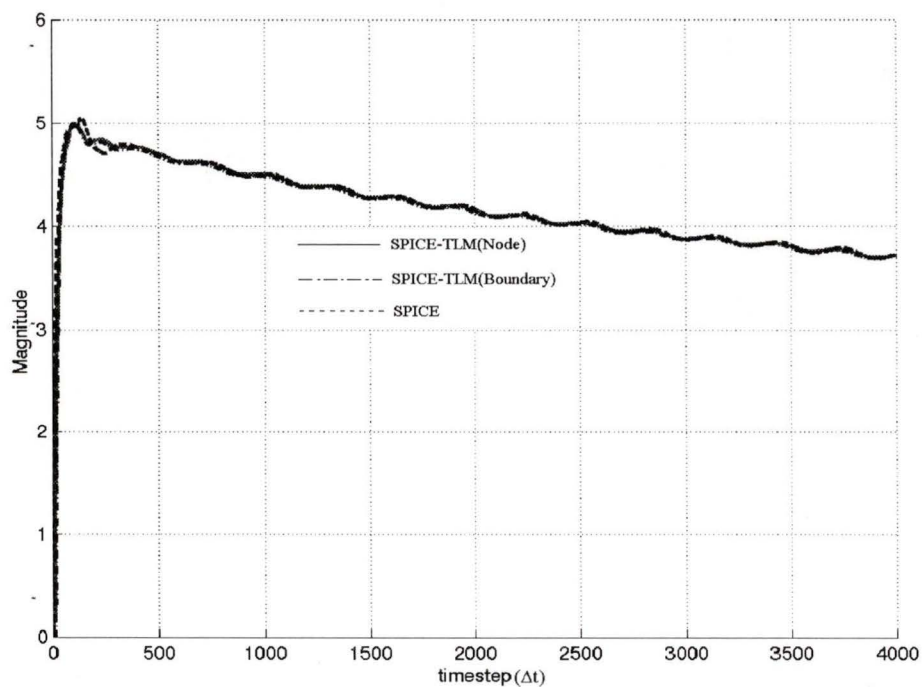


Figure 6.9 The collector-emitter voltage computed with SPICE alone (dotted line), SPICE-TLM using node implementation (solid line), and SPICE-TLM using boundary implementation (dash dotted line).

Figure 6.8 and 6.9 show the base-emitter voltage and the collector-emitter voltage at the transistor obtained with a full SPICE simulation and with a coupled 3D SPICE-TLM algorithm using node and boundary implementations, respectively. The slight differences in the results during the initial phase of the time response are due to the different implementations and reflect the differences in the reactive parasitics of the models.

The SPICE input file for the BJT is described below. Note that the saturation current (I_S) and the values of the capacitance are divided by the number of the sub-transistors.

```
VDC1 1 0 0
RI 1 2 282.56
% RI 1 2 1130.19 for boundary scheme
VI 2 3 0
QTR 4 3 0 AMP IC=0,0
VO 6 4 0
RC 6 7 282.56
% RC 6 7 1130.19 for boundary scheme
VDC2 7 0 0
.MODEL AMP NPN(IS=0.3333E-16 CJE=0.03333P CJC=0.03333P TF=0.1N TR=0.1N)
.TRAN 0.16678P 1.6678P UIC
.PRINT TRAN V(3,0) V(4,0) I(VI) I(VO)
.END
```

Note that the transistor in this thesis is inserted into the parallel-plate waveguide as in Figure 6.5. In this case, we can assume that the voltage at the transistor can be simply divided by the device height for obtaining the new voltages incident from the device upon the nodes. However, this assumption is not valid when the transistor is inserted into the microstrip line because of its fringe effect. Therefore, a generalized algorithm is required. This can be formulated using Eq 4.5.

6.4 Conclusion

A simple and very powerful method to connect SPICE with TLM was introduced in this chapter. Both one-port and two-port devices were modeled with 2D or 3D SPICE-TLM using node and boundary implementations. Excellent agreement has been achieved. It is seen that this method enables us to model much more complex structures with general nonlinear devices without the need for solving any nonlinear equations describing the behavior of the devices. However, the computational speed is slightly reduced as SPICE is called by TLM at each time step. The SPICE-TLM connection can be applied to star-type configuration.

Chapter 7

Discussion and Future Work

7.1 Introduction

It is not always advantageous or even possible to model a whole complex electromagnetic structure by a single numerical method since the required computational effort could be tremendous. A possible solution to this problem is to couple two available and appropriate numerical methods. The main benefit of such a hybrid combination of methods is that we can make use of their respective strengths to solve different parts of a complex electromagnetic problem and thus enhance computational efficiency.

The connection between SPICE and TLM is such a case in point. This hybrid system is very useful for solving electromagnetic field problems involving both linear and nonlinear devices. The integro-differential equations describing the behavior of the devices are solved by SPICE, and the field part is modeled with the TLM method.

In this thesis several techniques for embedding devices into a TLM network have been investigated and compared. While in previous studies [12][31] devices have been implemented exclusively using shunt stubs (device stubs), we have developed new techniques for boundary and star-type implementations.

The node implementation has the main advantage that the decoupling of the linear and nonlinear parts of the circuit can be achieved by choosing the appropriate admittance value of the device stub. The disadvantage of this approach is that the device stub introduces an extra reactance in the equivalent circuit of the device. However, this extra reactance can be eliminated by reducing the length of the device stub to zero. In this case, the stub admittance merely plays the role of a reference admittance for the interfacing between the TLM and SPICE variables.

The boundary embedding technique provides a scheme for connecting devices without using stubs. As a result, the computational effort is slightly reduced. This approach is realistic if the electromagnetic field does not penetrate into the device volume. However, if the device volume contains electromagnetic energy, the boundary model implementation introduces errors which must be compensated by adding appropriate reactive components to the equivalent circuit model of the device.

The star-type implementation uses a single lumped element to represent the device. As a result, the computational effort can be considerably reduced, particularly when modeling nonlinear elements, since the device equations need to be solved only once. At the same time the effect of parasitic embedding reactances can be reduced. It should be noted that the star-type implementation supposes that the connections between the device and the TLM ports are all of identical electrical length.

7.2 Future Work

We have explored the properties of the SPICE-TLM hybrid system. In this thesis, SPICE, version 2G6 first developed in 1970's, was coupled with the TLM algorithm. Since it is the oldest available version, some shortcomings became apparent. SPICE does not allow a user to measure directly the current flowing through a device. Independent sources must be connected in the SPICE input file. This may have been alleviated in newer versions of SPICE.

It is natural that the connection between SPICE and TLM reduces the computation speed since SPICE is called by TLM at each time step. The computation speed can be enhanced by using a flexible integration time step in SPICE, but this requires additional steps in the connection between the algorithms. For practical embedding of SPICE into TLM it will be necessary to provide a friendly user interface for entering a SPICE input file.

In this thesis, we have verified the SPICE-TLM algorithm by embedding linear and nonlinear devices into a simple structure. This algorithm has considerable potential for modeling complex electromagnetic structures such as MMICs. The distance between elements in an integrated MMIC circuit is very short. Therefore, SPICE can be employed to model those IC circuits using ideal transmission line elements. One additional advantage is that SPICE allows for the inclusion of thermal device properties and packaging parasitics.

It is important to note that the TLM-SPICE hybrid approach can deal with arbitrary waveforms and allows the inclusion of transients in the bias supply as shown in the various examples of Chapter 6.

7.3 Overall Conclusion

In this thesis we have studied embedding techniques that allow active and passive devices to be coupled to 2D and 3D TLM electromagnetic field models. We have focused on two fundamental concepts, namely

- 1) connection of devices to TLM nodes
- 2) connection of devices to TLM cell boundaries

We have implemented and compared both techniques and discussed their respective advantages and disadvantages. One of the main challenges is the formulation and discretization of the integro-differential equations that govern the behavior of complex nonlinear devices. There exists an extensive public domain software package (SPICE) for the time domain treatment of such devices and networks. It appears thus advantageous to connect this software to the TLM field algorithm for solving field problems with embedded devices.

The integration of SPICE and TLM is facilitated by the fact that TLM is already a circuit model of Maxwell's equations carrying voltage and current impulses. The connection of TLM with SPICE is thus straightforward and involves only a transformation between scattered and total voltage/current values via the characteristic admittance of the TLM link lines or stubs. The use of a separate program for device modeling allows the use of a different time step for the field and the device solvers, thus

potentially saving considerable computational effort. In fact, some problems are not amendable to solutions employing only TLM formulations. The availability of numerous library models in SPICE also represents a major bonus.

The examples given in this thesis confirm the advantages of the hybrid SPICE-TLM scheme, and results are virtually indistinguishable from analytical predictions provided that the errors due to the exclusion of field energy by the boundary implementation of finite volume devices are properly corrected. The results obtained in this thesis are sufficiently convincing to predict, that the embedding techniques can be used in the realization of field simulation tools for design purposes. The development of user-friendly interface features is beyond the scope of basic research, but it will certainly allow future designs to put the models developed in this thesis to good practical use.

Bibliography

- [1] M. N. O. Sadiku, "*Numerical Techniques in Electromagnetics*", CRC Press, Boca Raton, 1992
- [2] T. Itoh ed., "*Numerical Techniques for Microwave and Millimeter-Wave Passive Structures*", John Wiley & Sons, New York, 1989
- [3] W.J.R. Hofer, "*Some Thoughts on the Relationship between Finite Elements, Finite Differences and TLM*", Proceedings of the IEEE Antennas and Propagation Society International Symposium 1997 - Volume 2, V.2, 1997 -07 -13
- [4] P. B. Johns and R. L. Beurle, "*Numerical Solution of 2 Dimensional Scattering Problems using a Transmission Line Matrix*", Proceedings of the IEE, vol.118, no. 9, pp. 1203~1208, Sept. 1971
- [5] W. J. R. Hofer, "*The transmission-line matrix method—theory and applications*", IEEE Transactions on Microwave Theory and Techniques, vol. 33, no. 10, pp. 882-893, 1985
- [6] K. S. Yee, "*Numerical solution of initial boundary value problems involving Maxwell's equations in isotropic media*", IEEE Transactions on Antennas Propagation, vol. 14, no. 5, pp. 302-307, 1966
- [7] W. K. Gwarek, "*Analysis of arbitrarily shaped two-dimensional microwave circuits by finite-difference time-domain method*", IEEE Transactions on Microwave Theory and Techniques, vol. 36, no. 4, pp. 738-744, 1988

-
- [8] P. B. Johns, "On the relationship between TLM and finite-difference methods for Maxwell's equations", IEEE Transactions on Microwave Theory and Techniques, vol. 35, no. 1, pp. 60-61, 1987
- [9] W. K. Gwarek and P. B. Johns, "Comments on the relationship between TLM and finite-difference methods for Maxwell's equations", IEEE Transactions on Microwave Theory and Techniques, vol. 35, no. 9, pp. 872-873, 1987
- [10] R. H. Voelker and R. J. Lomax, "A finite-difference transmission line matrix method incorporating a nonlinear device model", IEEE Transactions on Microwave Theory and Techniques, vol. 38, no. 3, pp. 302-312, 1990
- [11] P. P. M. So, "Modeling of Complex Electromagnetic Structures with TLM--Theory and Practice--", Ph.D. Dissertation, University of Victoria, 1996
- [12] P. Russer, W. J. R. Hoefer, P. P. M. So, "Modeling of Nonlinear Active Regions in TLM", IEEE Microwave and Guided Letters, vol. 1, no. 1, pp. 10-13, Jan. 1991
- [13] B. Isele, P. Russer, "Modeling of Nonlinear Dispersive Active Elements in TLM", IEEE MTT-S International Microwave Symposium Digest, pp. 1217-1220, 1992
- [14] J. L. Herring, W. J. R. Hoefer, "Improved Excitation of 3D SCN TLM Based on Voltage Sources", IEEE MTT-S International Microwave Symposium, S. Francisco (CA), pp. 1031-1034, June. 1996
- [15] L. Albasha, C. M. Snowden, "New Integrated Simulation Techniques for the Electromagnetic Analysis of Microwave circuits Using the TLM method", Int. Journal of Numerical Modeling, vol. 9, no. 5, pp. 375-393, Sept-Oct. 1996

-
- [16] W. Sui, D. A. Christensen, "*Extending the Two-Dimensional FDTD Method to Hybrid Electromagnetic Systems with Active and Passive Lumped Elements*", IEEE Transactions on Microwave Theory and Techniques, vol. 40, no. 4, pp. 724-730, April. 1992
- [17] M. Piket-May, A. Taflove, J. Baron, "*FDTD Modeling of Digital Signal Propagation on 3D Circuits with Passive and Active Loads*", IEEE Transactions on Microwave Theory and Techniques, vol. 42, no. 8, pp. 1514-1523, August. 1994
- [18] V. A. Thomas, M. E. Jones, M. Piket-May, A. Taflove, E. Harrigan, "*The Use of SPICE Lumped Circuits as Sub-grid Models for FDTD Analysis*", IEEE microwave and Guided Letters, vol. 4, no. 5, pp. 141-143, May. 1994
- [19] P. B. Johns and R. L. Beurle, "*Numerical Solution of 2 Dimensional Scattering Problems using a Transmission Line Matrix*", Proceedings of the IEE, vol.118, no. 9, pp. 1203~1208, Sept. 1971
- [20] W. J. R. Hoefler and P. P. M. So, "*The mefisto-2D Theory*", Faustus Scientific Corporation, pp. 3~5, 1998
- [21] C. Christopoulos, "*The Transmission-Line Modeling Method TLM*", IEEE press. Piscataway. NJ, 1995
- [22] W. J. R. Hoefler and P. P. M. So, "*The Electromagnetic Wave Simulator*", John Wiley & Sons, Chichester, 1991

-
- [23] P. B. Johns, "A symmetrical condensed Node for the TLM Method", IEEE Transactions on Microwave Theory and Techniques, vol. 35, no. 4, pp. 370~377, April. 1987
- [24] J. L. Herring, C. Christopoulos, "Multigrid Transmission-Line Modeling Method For Solving Electromagnetic Field Problems", Electronic letters, 11th, July. 1991
- [25] S. Akhtarzad, P. B. Johns, "The solution of Maxwell's Equation in Three Space Dimensions and Time by the TLM Method of Numerical Analysis", Proc. IEE, vol. 122, no.12, pp. 1344~1348, Dec. 1975
- [26] M. Krumpholz and P. Russer, "On the Dispersion in TLM and FDTD", IEEE Transactions on Microwave Theory and Techniques, vol. 42, no. 7, pp. 1275~1279, July, 1994
- [27] L. De Menezes and W. J. R. Hoefer, "Accuracy of TLM Solutions of Maxwell's Equations", IEEE Transactions on Microwave Theory and Techniques, vol. 44, no. 12, pp. 2512~2518, Dec. 1996
- [28] P. Antognetti, G. Massobrio, "Semiconductor Device Modeling with SPICE", McGraw-Hill, New York, 1987
- [29] <http://www.pspice.com/upload/appnotes/PSPA022.html>
- [30] M. Al-Assadi, T.M. Benson, C. Christopoulos, "Interfacing field problems modeled by TLM to lumped circuits", Electronic letters, vol. 30, no. 4, pp. 290-191, Feb. 1994

-
- [31] L. Cascio, "*Modeling of nonlinear active and passive devices in three-dimensional TLM networks*", Ph.D. Dissertations, University of Victoria, 1998
- [32] G. Mur, "*Absorbing boundary conditions for the finite-difference approximation of the time-domain electromagnetic-field equations*", IEEE Trans. Electromagn. Compat., vol. 23, no. 4, pp. 377-382, 1981
- [33] J. H. Mathews, "*Numerical methods for computer science, engineering, and mathematics*", Prentice-Hall, 1987
- [34] http://www.repairfaq.org/ELE/F_Free_Spice2.html#FREESPACE_001
- [35] W. Banzhaf, "*Computer-Aided Circuit Analysis Using SPICE*", Prentice Hall, New Jersey, 1989
- [36] V. A. Thomas, M. E. Jones, M. Piket-May, A. Taflove, E. Harrigan, "*The Use of SPICE Lumped Circuits as Sub-grid Models for FDTD Analysis*", IEEE microwave and Guided Letters, vol. 4, no. 5, pp. 141-143, May. 1994
- [37] Berenger, J. P., "*A perfectly matched layer for the absorption of electromagnetic waves*", J. Computational Physics, Vol. 114, 1994, pp. 185-200

VITA

Surname: Park

Given Names: Jong Woon

Place of Birth: Yosu, Junranamdo, South Korea

Educational Institutions Attended:

University of Victoria 1999 to 2001

University of KyungHee 1994 to 1999

Degrees Awarded:

B. Eng. University of KyungHee 1999

Honours and Awards:

University of KyungHee Scholarship 1994 to 1999

University of Victoria Fellowship 1999 to 2001

Publications:

J.W. Park, P.P.M. So, W.J.R. Hoefer "Lumped and Distributed Device Embedding Techniques in Time Domain TLM Field Models", *IEEE MTT-S International Microwave Symposium*, vol. 3, pp. 2047~2050, May 2001

P.P.M. So, J.W. Park, W.J.R. Hoefer "A Generalized Cell-Boundary Framework for Modeling of Devices and Conductors", *URSI-B2001*, MN-T04.09, pp. 408~410

P.P.M. So, W. Liu, J.W. Park, W.J.R. Hoefer "Application of Coupled TLM-Thermal Analysis to Devices Embedded in Waveguides", *CEM-TD Workshop*, September 2001

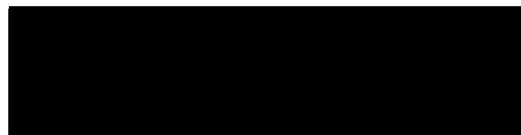
UNIVERSITY OF VICTORIA PARTIAL COPYRIGHT LICENSE

I hereby grant the right to lend my thesis to users of the University of Victoria Library, and to make single copies only for such users or in response to a request from the Library of any other university, or similar institution, on its behalf or for one of its users. I further agree that permission for extensive copying of this thesis for scholarly purposes may be granted by me or a member of the University designated by me. It is understood that copying or publication of this thesis for financial gain by University of Victoria shall not be allowed without my written permission.

Title of Thesis:

Lumped and Distributed Device Embedding Techniques in Time Domain TLM Field Models

Author



Jong Woon Park
August 15, 2001